Materials Fundamentals of Gate Dielectrics

Edited by
Alexander A. Demkov and
Alexandra Navrotsky

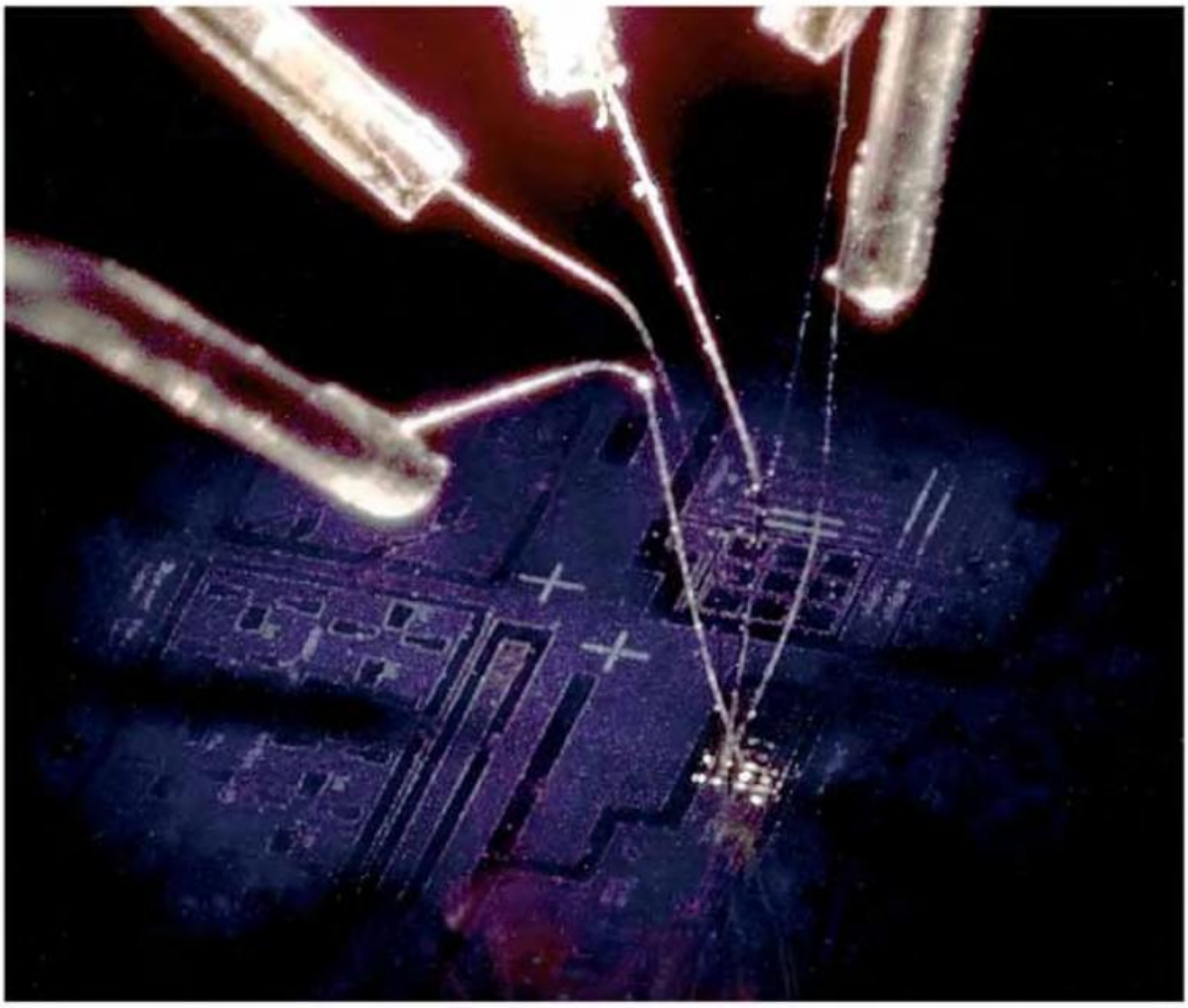

Springer

Chapter 7

IVB TRANSITION METAL OXIDES AND SILICATES: AN AB INITIO STUDY

GIAN-MARCO RIGNANESE

Unité de Physico-Chimie et de Physique des Matériaux,
Université Catholique de Louvain,
1 Place Croix du Sud, B-1348 Louvain-la-Neuve, Belgium

ABSTRACT

Using density-functional theory, we investigate the structural, vibrational and dielectric properties of group IVb transition metals (M = Hf, Zr, Ti) oxides and silicates which have drawn considerable attention as alternative high-k materials. For the oxides, three crystalline phases of dioxide are considered. The first two are the cubic and tetragonal structures which exist for hafnia HfO_2 or zirconia ZrO_2, while it is hypothetical for titania TiO_2. The third one is the rutile structure, which on the contrary is the naturally occurring phase of titania, while it is hypothetical for hafnia and zirconia. For the silicates, we analyze first the crystalline phases: hafnon $HfSiO_4$, zircon $ZrSiO_4$ and an hypothetical $TiSiO_4$ structure. Finally, we consider the amorphous silicates. We introduce a scheme which relates the dielectric constants to the local bonding of Si and metal atoms, based on the definition of parameters characteristic of the basic structural units centered on Si and metals atoms and including their nearest O neighbors. This scheme which considerably reduces the computational cost of the calculations allows one to treat much larger systems. Applied to amorphous Zr silicates, it provides a good description of the measured dielectric constants, both of the optical and the static ones.

INTRODUCTION

The key challenge of computational condensed matter physics is to predict the properties of all kinds of materials. In this respect, one of the most successful approaches is the density-functional theory (DFT), which describes very accurately not only standard bulk materials but also complex systems such as proteins and carbon nanotubes.

A.A. Demkov and A. Navrotsky (eds.), Materials Fundamentals of Gate Dielectrics, 249–290.

In the framework of the quest for high-k materials to replace conventional SiO_2 as the gate dielectric in MOS devices, first-principles calculations constitute a valuable tool to understand the behavior of novel materials at the atomic scale without requiring empirical data. This is particularly interesting for the early stages of research when relatively little experimental data are available. In terms of its predictive accuracy, density-functional theory has proven to be very appropriate to study the ground-state properties of the electronic system, such as the structural, vibrational, and dielectric properties on which we will focus in this chapter.

However, DFT calculations have one important drawback associated to their high computational cost, which limits both the length and time scales of the phenomena which can be modeled. Nowadays, it is possible to treat systems containing up to hundreds of atoms within the most widespread DFT approach based on plane-wave basis sets and pseudopotentials. For the high-k materials that we consider here, it is important to note that transition-metal and first-row elements (e.g., oxygen) generally present an additional difficulty when treated with plane-wave basis sets. Namely, their valence wave functions are generally strongly localized around the nucleus and may require a large number of basis functions to be described accurately, thus further limiting the size of the system that can be investigated.

This chapter is dedicated to the first-principles study of the group IVB transition metal oxides and silicates which have drawn considerable attention as alternative high-k materials. Indeed, these systems have shown much promise in overall materials properties (1). On the one hand, the TiO_2 system is attractive due to its anomalously high permittivity (2–5). On the other hand, HfO_2 and ZrO_2 as well as the silicates $HfSiO_4$ and $ZrSiO_4$ in the form of amorphous films are stable in direct contact with Si up to high temperature, which is highly desirable to avoid the degradation of the interface properties by formation of a low-k interfacial layer (6, 7). In fact, the Hf–Si–O and Zr–Si–O phase diagram present a large phase field of stable silicates (a detailed discussion can be found in the chapter by Navrotsky and Ushakov); while, on the contrary, for the Ti–Si–O system, there is little mutual solubility between TiO_2 and SiO_2. Recently, however titanium silicates have also been stabilized and considered as a potential alternative for SiO_2 (8–10). The idea is to increase the static permittivity ϵ_0 with the amount of Hf, Zr, or Ti incorporated into the silicate film. In order to be able to control this process, it is highly desirable to develop an understanding of how the permittivity of Hf, Zr, and Ti silicates are affected by the underlying microscopic structure.

This chapter is organized as follows. In Section 1, we briefly describe the main results of the density functional theory and present the principal equations related to the properties that will be analyzed in the subsequent sections. We also provide some technical details about the calculations. Section 2 is devoted to the study of structural, vibrational and dielectric properties of hafnia (HfO_2), zirconia (ZrO_2), and titania (TiO_2). Three crystalline phases are considered: the cubic, the tetragonal, and the rutile structures. The differences and the analogies between the three phases and between hafnia, zirconia, and titania are presented in details. In Section 3, the structural and electronic properties of the crystalline silicates $MSiO_4$ (with M = Hf, Zr, Ti) are

investigated. We discuss their Born effective charge tensors and compare the phonon frequencies at the Γ point. A detail analysis of the dielectric permittivity tensors is presented. Section 4 is dedicated to the study of amorphous silicates. For this purpose, a scheme is introduced which relates the dielectric constants to the local bonding of Si and M (= Hf, Zr, Ti) atoms. The central idea is to define of characteristic parameters for the basic structural units (SUs) formed by Si and M (= Hf, Zr, Ti) atoms and their nearest neighbors. With this scheme, heavy large-scale calculations, which are beyond current computational capabilities, are avoided. Applied to amorphous Zr silicates, our scheme provides a good description of the measured dielectric constants, both of the optical and the static ones. Finally, in Section 5, we present our conclusions.

1. THEORETICAL BACKGROUND

1.1. Ground State Properties

The key concept of density functional theory is to describe an interacting system of electrons through the density rather than through the many-body wavefunction. For a solid with N electrons obeying the Pauli principle and interacting via the Coulomb potential, the complexity of the problem is reduced from $3N$ degrees of freedom for the many-body wavefunction to only three (the spatial coordinates x, y, and z).

Firstly, Hohenberg and Kohn (11) showed that the ground state of the electron system is completely defined by the electron density which minimizes the total energy. Furthermore, they demonstrated that all the other ground state properties of the system (e.g., the lattice constant, the cohesive energy, etc.) are functionals of the ground state electron density. Consequently, once the ground state electron density is known, all the other ground state properties follow (in principle, at least).

Later on, Kohn and Sham (12) proved that this variational approach is equivalent to equations of a very simple form:

$$(T + v_{\mathrm{KS}}[n])\,|\psi_\alpha\rangle = (T + v_{\mathrm{ext}} + v_{\mathrm{H}}[n] + v_{\mathrm{xc}}[n])\,|\psi_\alpha\rangle = \epsilon_\alpha |\psi_\alpha\rangle, \tag{1}$$

known today as the Kohn–Sham equations. These effectively single-particle eigenvalue equations are formally similar to the time-independent Schroedinger equation, T being the kinetic energy operator and v_{KS} the potential experienced by the electrons. The latter is usually decomposed into a part which is external to the electronic system v_{ext}, for instance the electron–ion interaction, and a part describing the electron–electron interactions. For convenience, the last part is further split into the Hartree potential v_{H} and the exchange-correlation potential v_{xc}, whose form is, in general, unknown.

The ground state energy of the electronic system is given by:

$$E_{\mathrm{el}}\{\psi_\alpha\} = \sum_{\alpha}^{\mathrm{occ}} \langle \psi_\alpha | T + v_{\mathrm{ext}} | \psi_\alpha \rangle + E_{\mathrm{Hxc}}[n], \tag{2}$$

where $E_{\rm Hxc}$ is the Hartree and exchange-correlation energy functional of the electron density $n(\mathbf{r})$ with $\delta E_{\rm Hxc}/\delta n = v_{\rm H} + v_{\rm xc}$, and the summation runs over the occupied states α. The occupied Kohn–Sham orbitals are subject to the orthonormalization constraints,

$$\int \psi_\alpha^*(\mathbf{r})\psi_\beta(\mathbf{r})\mathrm{d}\mathbf{r} = \langle\psi_\alpha|\psi_\beta\rangle = \delta_{\alpha\beta}, \tag{3}$$

where α and β label occupied states. The density is obtained from

$$n(\mathbf{r}) = \sum_\alpha^{\rm occ} \psi_\alpha^*(\mathbf{r})\psi_\alpha(\mathbf{r}). \tag{4}$$

Presently, DFT is considered as the method of choice for simulating solids and molecules from first-principles. The interested reader may find a collection of some interesting DFT applications in the review article of Pickett (13). For more technical details about DFT, we recommend the review article of Payne et al. (14).

1.2. Response Properties

In this brief overview, we will only present the *responses* of solid systems to two types of perturbations: (a) collective displacements of atoms characterized by a wavevector $\mathbf{q}$ (phonons) and (b) homogeneous static electric fields. These responses can also be obtained in the framework of DFT using various methods, which can be found in the nice review article by Baroni et al. (15).

The method that is adopted in the calculations described here is based on a variational approach to density-functional perturbation theory, which is presented in details in refs. (16, 17). The first paper (16) is devoted to the computation of the first-order derivatives of the wavefunctions, density and self-consistent potential with respect to the perturbations mentioned above; while the second paper (17) presents the second-order derivatives. We adopt the same notations as in those references to introduce the properties that are studied in the following sections. In particular, κ and α run over the atoms in the unit cell and over the three cartesian directions, respectively; $\tau_{\kappa\alpha}$ denote the equilibrium positions.

The squares of the phonon frequencies $\omega_{m\mathbf{q}}^2$ at $\mathbf{q}$ are determined as eigenvalues of the dynamical matrix $\tilde{D}_{\kappa\alpha,\kappa'\beta}(\mathbf{q})$, or as solutions of the following generalized eigenvalue problem:

$$\sum_{\kappa'\beta} \tilde{C}_{\kappa\alpha,\kappa'\beta}(\mathbf{q})U_{m\mathbf{q}}(\kappa'\beta) = M_\kappa \omega_{m\mathbf{q}}^2 U_{m\mathbf{q}}(\kappa\alpha), \tag{5}$$

where M_κ is the mass of the ion κ, and the matrix $\tilde{C}$ is related to the dynamical matrix $\tilde{D}$ through:

$$\tilde{D}_{\kappa\alpha,\kappa'\beta}(\mathbf{q}) = \frac{\tilde{C}_{\kappa\alpha,\kappa'\beta}(\mathbf{q})}{(M_\kappa M_{\kappa'})^{1/2}}. \tag{6}$$

The matrix $\tilde{C}_{\kappa\alpha,\kappa'\beta}(\mathbf{q})$ is the Fourier transform of the matrix of the interatomic force constants. It is connected to the second-order derivative of the total energy with respect to collective atomic displacements (17).

The limit $\mathbf{q} \to \mathbf{0}$ must be performed cautiously (17) by the separate treatment of the macroscopic electric field associated with phonons in this limit. A bare dynamical matrix at $\mathbf{q} = \mathbf{0}$ is first calculated, then a non-analytical part is added, in order to reproduce correctly the $\mathbf{q} \to \mathbf{0}$ behavior along different directions:

$$\tilde{C}_{\kappa\alpha,\kappa'\beta}(\mathbf{q} \to \mathbf{0}) = \tilde{C}_{\kappa\alpha,\kappa'\beta}(\mathbf{q} = \mathbf{0}) + \tilde{C}^{\mathrm{NA}}_{\kappa\alpha,\kappa'\beta}(\mathbf{q} \to \mathbf{0}). \tag{7}$$

The expression of the non-analytical part will be presented later on in this section.

For insulators, the dielectric permittivity tensor is defined as the coefficient of proportionality between the macroscopic displacement field and the macroscopic electric field, in the linear regime:

$$\mathcal{D}_{\mathrm{mac},\alpha} = \sum_{\beta} \epsilon_{\alpha\beta} \mathcal{E}_{\mathrm{mac},\beta}. \tag{8}$$

It can be obtained as

$$\epsilon_{\alpha\beta} = \frac{\partial \mathcal{D}_{\mathrm{mac},\alpha}}{\partial \mathcal{E}_{\mathrm{mac},\beta}} = \delta_{\alpha\beta} + 4\pi \frac{\partial \mathcal{P}_{\mathrm{mac},\alpha}}{\partial \mathcal{E}_{\mathrm{mac},\beta}}. \tag{9}$$

In general, the displacement $\mathcal{D}_{\mathrm{mac}}$, or the polarization $\mathcal{P}_{\mathrm{mac}}$, will include contributions from ionic displacements. In the presence of an applied field of high frequency, the contribution to the dielectric permittivity tensor resulting from the electronic polarization, usually noted $\epsilon^{\infty}_{\alpha\beta}$, dominates. This ion-clamped dielectric permittivity tensor is related to the second-order derivatives of the energy with respect to the macroscopic electric field (17). Later on in this section, we will consider the supplementary contributions to the polarization coming from the ionic displacements.

For insulators, the Born effective charge tensor $Z^{*}_{\kappa,\beta\alpha}$ is the proportionality coefficient relating, at linear order, the polarization per unit cell, created along the direction β, and the displacement along the direction α of the atoms belonging to the sublattice κ, under the condition of zero electric field. The same coefficient also describes the linear relation between the force on an atom and the macroscopic electric field:

$$Z^{*}_{\kappa,\beta\alpha} = \Omega_0 \frac{\partial \mathcal{P}_{\mathrm{mac},\beta}}{\partial \tau_{\kappa\alpha}(\mathbf{q} = \mathbf{0})} = \frac{\partial F_{\kappa,\alpha}}{\partial \mathcal{E}_{\beta}} \tag{10}$$

where Ω_0 is the volume of the primitive unit cell. The Born effective charge tensors are connected to the mixed second-order derivative of the energy with respect to atomic displacements and macroscopic electric field (17).

Finally, we present two phenomena that arise from the same basic mechanism: the coupling between the macroscopic electric field and the polarization associated with the $\mathbf{q} \to \mathbf{0}$ atomic displacements. In both cases, the Born effective charges are involved.

On the one hand, in the computation of the low-frequency (infrared) dielectric permittivity tensor, the response of the ions must be include. Their motion will be

triggered by the force due to the electric field, while their polarization will be created by their displacement.

At the lowest order of approximation in the theory, the macroscopic frequency-dependent dielectric permittivity tensor $\epsilon_{\alpha\beta}(\omega)$ is calculated as follows:

$$\epsilon_{\alpha\beta}(\omega) = \epsilon^{\infty}_{\alpha\beta} + \frac{4\pi}{\Omega_0} \sum_m \frac{S_{m,\alpha\beta}}{\omega_m^2 - \omega^2}, \tag{11}$$

where the mode-oscillator strength $S_{m,\alpha\beta}$ is defined as:

$$S_{m,\alpha\beta} = \Big(\sum_{\kappa\alpha'} Z^*_{\kappa,\alpha\alpha'} U^*_{m\mathbf{q}=\mathbf{0}}(\kappa\alpha')\Big)\Big(\sum_{\kappa'\beta'} Z^*_{\kappa',\beta\beta'} U_{m\mathbf{q}=\mathbf{0}}(\kappa'\beta')\Big). \tag{12}$$

A damping factor might be added to Eq. (11) in order to take into account anharmonic effects, and fit frequency-dependent experimental data. For our purpose, such a damping factor can be ignored.

At zero frequency, the static dielectric permittivity tensor is usually noted $\epsilon^0_{\alpha\beta}$; it is obtained by:

$$\epsilon^0_{\alpha\beta} = \epsilon^{\infty}_{\alpha\beta} + \sum_m \Delta\epsilon_{m,\alpha\beta} = \epsilon^{\infty}_{\alpha\beta} + \frac{4\pi}{\Omega_0} \sum_m \frac{S_{m,\alpha\beta}}{\omega_m^2}. \tag{13}$$

In parallel to this decomposition of the static dielectric tensor, one can define a mode-effective charge vector:

$$Z^*_{m,\alpha} = \frac{\sum_{\kappa\beta} Z^*_{\kappa,\alpha\beta} U_{m\mathbf{q}=\mathbf{0}}(\kappa\beta)}{\Big(\sum_{\kappa\beta} U^*_{m\mathbf{q}=\mathbf{0}}(\kappa\beta) U_{m\mathbf{q}=\mathbf{0}}(\kappa\beta)\Big)^{1/2}}. \tag{14}$$

This vector is related to the global polarization resulting from the atomic displacements for a given phonon mode m. The non-zero components reveal the directions in which the mode is infrared active.

On the other hand, for phonons in the long-wavelength limit, a macroscopic polarization and electric field can be associated with the atomic displacements. At the simplest level of theory, the phonon eigenfrequencies then depend on the direction along which the limit is taken as well as on the polarization of the phonon. This gives birth to the LO–TO splitting, and to the Lyddane–Sachs–Teller relation (17).

For insulators, the non-analytical, direction-dependent part of the dynamical matrix $\tilde{C}^{\mathrm{NA}}_{\kappa\alpha,\kappa'\beta}(\mathbf{q} \to \mathbf{0})$ is given by:

$$\tilde{C}^{\mathrm{NA}}_{\kappa\alpha,\kappa'\beta}(\mathbf{q} \to \mathbf{0}) = \frac{4\pi}{\Omega_0} \frac{\Big(\sum_\gamma q_\gamma Z^*_{\kappa,\gamma\alpha}\Big)\Big(\sum_{\gamma'} q_{\gamma'} Z^*_{\kappa',\gamma'\beta}\Big)}{\sum_{\alpha\beta} q_\alpha \epsilon^{\infty}_{\alpha\beta} q_\beta}. \tag{15}$$

Hence, once the dynamical matrix at $\mathbf{q} = \mathbf{0}$ as well as $\epsilon^{\infty}_{\alpha\beta}$ and the Born effective charges tensors are available, it is possible to compute the LO–TO splitting of phonon frequencies at $\mathbf{q} = \mathbf{0}$.

1.3. Technical Details

We have performed all the calculations using the ABINIT package, developed by the authors and collaborators (18). The exchange-correlation energy is evaluated within the local density approximation (LDA) to density-functional theory, using Perdew–Wang's parameterization (19) of Ceperley–Alder electron-gas data (20).

Only valence electrons are explicitly considered using pseudopotentials to account for core-valence interactions. We use norm-conserving pseudopotentials (21,22) with Hf(5s, 5p, 5d, 6s), Zr(4s, 4p, 4d, 5s), Ti(3s, 3p, 3d, 4s), Si(3s, 3p), and O(2s, 2p) levels treated as valence states. The following atomic valence configurations are used to generate the pseudopotentials: for Hf, $5s^2 5p^6 5d^2 6s^2$; for Zr, $4s^2 4p^6 4d^2 5s^0$; for Ti, $3s^2 4p^6 3d^2 4s^0$; for Si, $3s^2 3p^2$; and for O, $2s^2 2p^4$. In the case of Hf, we take core radii of 1.50, 2.85, 2.45, 3.50 a.u. for describing angular waves from s to f. The corresponding values (up to the d wave) are 1.75, 1.55, and 1.70 a.u. for the Zr pseudopotential, and 1.25, 1.25, and 1.65 a.u. for the Ti pseudopotential. For the Si pseudopotential, the same cutoff radius of 2.00 a.u. is used for the three lowest angular-momentum waves. For the O pseudopotential, we use a cutoff radius of 1.50 a.u. for both s and p waves. We adopted a separable form for the pseudopotentials (23) treating the following angular-momentum waves as local: f for Hf, d for Zr, d for Ti, d for Si, and p for O.

The wavefunctions are expanded in plane waves up to a kinetic energy cutoff of 30 Ha for Hf- and Zr-based systems and of 45 Ha for Ti-based systems. For each crystalline system, the Brillouin zone is sampled by a Monkhorst–Pack (24) mesh of k-points. For the cubic and tetragonal phases of the oxides as well as for the crystalline silicates, our mesh corresponds to a $4 \times 4 \times 4$ grid in the conventional unit cell, leading to 10, 12, and 15 special k-points in the irreducible Brillouin zone, respectively. For the rutile phase of the oxides, we use a $4 \times 4 \times 6$ grid that results in nine special k-points in the irreducible Brillouin zone. For the amorphous system, we only use the Γ-point to sample the Brillouin zone. The chosen kinetic energy cutoff and k-point sampling of the Brillouin zone ensure convergence of all the calculated properties.

2. CRYSTALLINE OXIDES

2.1. Introduction

Titania (TiO_2) is by far the most important compound formed by the elements of group IVB, its importance arising predominantly from its use as a white pigment. Three forms exists at room temperature: rutile, anatase, and brookite. Each of them occurs naturally. The rutile is the most common form, both in nature and as produced commercially. It is also the most stable phase: the other transform into it on heating. Note also that all three forms contain sixfold coordinated titanium atoms.

Hafnia (HfO_2) and zirconia (ZrO_2) undergo polymorphic transformations with changes in external parameters. At high temperature, the compounds are highly defective and their structure is fluorite type ($Fm\bar{3}m$). The decreasing temperature induces a cubic to tetragonal ($P4_2/nmc$) phase transition ($c - t$) at about 2650°C for

HfO_2 (25) and about 2350°C for ZrO_2 (26). This transition is followed by a tetragonal to monoclinic ($P2_1/c$) martensitic phase transition ($t - m$) at about 1650°C for hafnia (27) and about 1150°C for zirconia (28). In the cubic and tetragonal phase, the metal atoms are eightfold coordinated while in the monoclinic phase they are sevenfold coordinated. None of the existing phases have sixfold coordinated atoms as in the rutile structure.

Hafnia and zirconia have many similar physical and chemical properties, but they differ considerably from titania (e.g., difference in the stable phase). This can be related to the very close chemical homology between Hf and Zr, compared to Ti.

Considering the valence electrons only, the electron configurations of Hf, Zr, and Ti differ only by the principal number of the occupied orbitals it is $5d^26s^2$ for hafnium, $4d^25s^2$ for zirconium, and $3d^24s^2$ for titanium. Thus, in principle, they should be characterized by decreasing electronegativities and increasing atomic and ionic radii from Ti to Hf. However, in the periodic table, the inner transition (rare-earth) elements immediately preceding Hf add electrons to the inner 4f shell from element N° 58, cerium, to N° 71, lutetium (it would actually be more correct to write that the electron configuration of hafnium is $4f^{14}5d^26s^2$). Because the nuclear charge increases while no additional outer shells are filled, there is a contraction in the atomic size. Consequently, the element N° 72, hafnium, has a slightly smaller atomic size than element N° 40, zirconium, the group IVB element in the preceding row. This results in the so-called lanthanide contraction.

As a result, while the atomic radius of Ti (1.40 Å) is indeed smaller than for Zr (1.55 Å), the atomic radius of Hf (1.55 Å) is identical to that of Zr (29). The ionic radii (M^{4+}) also presents the same anomaly: it is smaller for Ti (0.61 Å) than for Zr (0.84 Å), but it is essentially the same for the latter and Hf (0.84 Å) (30). Finally, their electronegativities also show an anomalous trend with values of 1.23 for hafnium and 1.22 for zirconium, compared to 1.32 for Ti (31). All this explains the origin of the close similarity between HfO_2 and ZrO_2 with respect to TiO_2.

The structural, electronic and dynamical properties of hafnia, zirconia, and titania have been the object of several first-principles studies (32–46). For sake of brevity, we here only present here our results for the cubic, tetragonal, and rutile phases.

2.2. Structural Properties

To model the crystalline oxides, we consider the cubic, tetragonal, and rutile structures which are illustrated in Fig. 1. For HfO_2 and ZrO_2, the cubic and tetragonal phases exist in nature, while the rutile phase is purely hypothetical. On the contrary, for TiO_2, the rutile occurs naturally, while the other two are hypothetical.

The cubic phase takes the fluorite structure (space group $Fm\bar{3}m$, N° 225), which is fully characterized by a single lattice constant a. The M (= Hf, Zr) atoms are in a face-centered-cubic structure and the O atoms occupy the tetrahedral interstitial sites associated with this fcc lattice. The primitive unit cell contains one formula unit of MO_2 with M (= Hf, Zr, Ti), while the conventional unit cell has four of them.

The tetragonal phase (space group $P4_2/nmc$, N° 137) can be viewed as a distortion of the cubic structure obtained by displacing alternating pairs of O atoms up and down

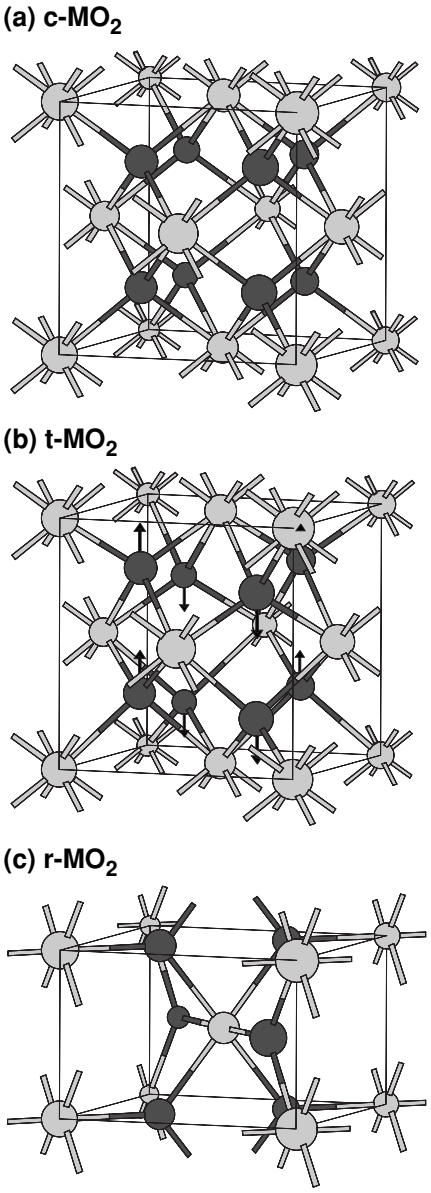

Fig. 1. Structures of the cubic and tetragonal phases of HfO_2, ZrO_2, and TiO_2. A ball and stick representation is adopted where M (= Hf, Zr, Ti) and O atoms are colored in light and medium grey, respectively. For the tetragonal phase, the arrows indicate the displacements of oxygen pairs relative to the cubic structure.

by an amount Δz along the z direction, as marked by the arrows in Fig. 1, and by applying a tetragonal strain. The resulting primitive cell is doubled compared to the cubic phase, including two formula units of MO_2. The conventional unit cell, which is reproduced in in Fig. 1(b), has four formula units of MO_2 with M = (Hf, Zr, Ti). The tetragonal structure is completely specified by two lattice constants (a and c) and the dimensionless ratio $d_z = \Delta z/c$ describing the displacement of the O atoms. The cubic phase can be considered as a special case of the tetragonal structure with $d_z = 0$ and $c/a = 1$ (if the primitive cell is used for the tetragonal phase, $c/a = \sqrt{2}$).

The rutile structure (space group $P4_2/mnm$, N° 136) has a tetragonal unit cell with two formula units of MO_2 with M (= Hf, Zr, Ti). The metal atoms occupy the body-centered-cubic positions and the O atoms are at $(u, u, 0)$, $(1-u, 1-u, 0)$, $(\frac{1}{2}-u, \frac{1}{2}+u, \frac{1}{2})$, and $(\frac{1}{2}+u, \frac{1}{2}-u, \frac{1}{2})$, as reported in Fig. 1(c). The rutile structure is completely specified by two lattice constants (a and c) and the internal parameter u related to the position of O atoms.

For hafnia and zirconia, the tetragonal phase is found to be the most stable with $E_t < E_c < E_r$, at variance with titania for which it is the rutile phase which is energetically favored with $E_r < E_t < E_c$. It is interesting to note that in the rutile phase the M (= Ti, Zr, Hf) atoms are sixfold coordinated while in the cubic and tetragonal phases they are eightfold coordinated. This is a first clear difference between Ti atoms on the one hand, and Zr and Hf atoms on the other. It can be related to the smaller ionic radius of Ti^{4+} (0.61 (47)) compared to Zr^{4+} and Hf^{4+} (0.72 and 0.71 Å, respectively (47)).

Our calculated structural parameters for the cubic, tetragonal, and phases of HfO_2, ZrO_2, and TiO_2 are reported in Table 1. For the naturally occurring, the agreement with the experimental values (28, 48). is very good: the errors on the lattice constants and the volumes are smaller than 2%, as is typical for LDA calculations. The largest discrepancy is for d_z in t-ZrO_2 (the small displacement from the cubic phase localization): our value is about 30% smaller than the experimental data, but it is in excellent agreement with the results of other first-principles calculations. The discrepancy with experiment is probably due to the fact that our calculations are performed at zero-temperature.

While the structural parameters for Zr and Hf based oxides are very similar, the values for Ti based materials can differ by about 5–10% from the former two. The largest difference is observed in the tetragonal phase in which the Ti–O distance is found to be 10 and 13% smaller than the Zr–O and Hf–O distances, respectively. This is another evidence of the different chemistry of 3d metals with respect to 4d and 5d metals.

2.3. Born Effective Charge Tensors

In Table 2, we report non-vanishing components of the calculated Born effective charge tensors for M (= Hf, Zr, Ti) and O atoms in the cubic, tetragonal, and rutile phases of hafnia, zirconia, and titania. These values should be compared with the nominal ionic charges $Z = +4$ for M (= Hf, Zr, Ti) atoms and $Z = -2$ for O atoms.

Table 1. Structural parameters for the cubic (c), tetragonal (t), and rutile (r) phases of HfO_2, ZrO_2, and TiO_2

	HfO_2	ZrO_2	TiO_2
c			
a	5.11	5.01	4.72
Volume	33.36	31.44	26.29
d(M–O)	2.21	2.17	2.04
t			
a	5.11	5.02	4.71
c	5.17	5.09	4.93
d_z	0.0310	0.0400	0.0701
Volume	33.75	32.07	27.34
d(M–O)	2.13	2.07	1.89
	2.32	2.31	2.29
r			
a	4.90	4.80	4.53
c	3.27	3.22	2.92
u	0.3051	0.3054	0.3033
Volume	78.51	74.19	60.12
d(M–O)	2.11	2.07	1.93
	2.12	2.08	1.94

The lengths are expressed in Å.

Due to the symmetry of the cubic phase, the Born effective charge tensors of M (= Hf, Zr) and O atoms are diagonal and isotropic. The value of Z^* is anomalously large for M (= Hf, Zr, Ti) atoms compared to the nominal ionic charge $Z = 4$. This behavior has also been observed in the case of $PbZrO_3$ (49). A detailed analysis of the physics of Born effective charges in the case of perovskite ferroelectrics (like $PbZrO_3$) ascribed this effect to a mixed covalent–ionic bonding (50).

In the tetragonal structure, the symmetry imposes that the Born effective charge tensor of M (= Hf, Zr, Ti) atoms is diagonal and only has two independent components: parallel ($Z^*_\parallel$) and perpendicular ($Z^*_\perp$) to the *c* axis. For hafnia and zirconia, the tensors are quite isotropic. The value of $Z^*_\perp$ is identical to the one calculated for the cubic phase, while $Z^*_\parallel$ is 6 and 10% smaller for HfO_2 and ZrO_2, respectively. For titania, the tensor is very anisotropic: the value of $Z^*_\perp$ is 3% larger than the one calculated for the cubic phase, while $Z^*_\parallel$ is more than 30% smaller. This is another manifestation of the different behavior of Ti atoms compared to Zr and Hf atoms. The Born effective charge tensor of O atoms is also diagonal, but with three independent components. It is quite anisotropic for all three systems. In t-TiO_2, it is even more anisotropic than the tensor of Ti atoms: the ratio between the largest and the smallest components is about 2.5. This ratio is only 1.6 for t-ZrO_2 and 1.4 for t-HfO_2. Such a strong anisotropy of the Born effective charge tensor for O atoms has already been observed in SiO_2-stishovite (51).

Table 2. Non-vanishing components of the calculated Born effective charge tensors for M (= Hf, Zr, Ti) and O atoms in the cubic (c), tetragonal (t), and rutile (r) phases of HfO_2, ZrO_2, and TiO_2

Atom	HfO_2	ZrO_2	TiO_2
c			
M	(+5.58 +5.58 +5.58)	(+5.74 +5.74 +5.74)	(+6.40 +6.40 +6.40)
O	(−2.79 −2.79 −2.79)	(−2.87 −2.87 −2.87)	(−3.20 −3.20 −3.20)
t			
M	(+5.57 +5.57 +5.24)	(+5.74 +5.74 +5.15)	(+6.63 +6.63 +4.42)
O	(−3.22 −2.35 −2.62)	(−3.51 −2.24 −2.57)	(−4.76 −1.94 −2.21)
r			
M	(+5.38 +0.66 +6.31)	(+5.58 +0.69 +6.51)	(+6.36 +1.00 +7.52)
	[+6.04 +4.72 +6.31]	[+6.27 +4.89 +6.51]	[+7.36 +5.36 +7.52]
O[a]	(−2.69 −1.37 −3.15)	(−2.79 −1.46 −3.25)	(−3.18 −1.81 −3.76)
	[−4.06 −1.32 −3.15]	[−4.25 −1.33 −3.25]	[−4.99 −1.37 −3.76]

For the cubic and tetragonal phases, the tensors are diagonal, only the principal elements are given. For the rutile phase, the three independent components ($Z^*_{xx} = Z^*_{yy}$, $Z^*_{xy} = Z^*_{yx}$, and Z^*_{zz}) of the tensors are given, and the principal components are indicated between brackets.
[a] For the rutile phase, the components for O atoms in the rutile phase refer to the atom located at (u, u, 0). The corresponding values for the other oxygen atoms can be obtained using the symmetry operations.

In the rutile structure, the Born effective charge tensors of M (= Hf, Zr, Ti) or O atoms have only three independent components: Z^*_{xx}, Z^*_{xy}, and Z^*_{zz}. Indeed, Z^*_{yy} and Z^*_{yx} are equal to Z^*_{xx} and Z^*_{xy}, respectively, while the other components are zero. When we take a coordinate system whose axes are along the [110], [1$\bar{1}$0], and [001] directions, the tensors are diagonalized. The principal values obtained in this coordinate system are reported between brackets in Table 2. For the metal atoms, the ratio between the largest and the smallest components is about 1.3 in r-HfO_2, 1.3 for r-ZrO_2, and 1.4 for r-TiO_2. For O atoms, this ratio is 3.1 for hafnia, 3.2 for zirconia, and 3.6 for titania. Thus, the anisotropy is even larger than in the tetragonal phase, especially for O atoms in hafnia and zirconia.

It is interesting to note that the Born effective charges of c-HfO_2 are about 3% smaller (in absolute value) than those of c-ZrO_2 which are in turn more than 11% smaller than those of c-TiO_2. The comparison between the Z^* values in the tetragonal phases of hafnia, zirconia, and titania is also very instructive. In directions perpendicular to the c axis, the Born effective charges of the M (= Hf, Zr, Ti) atoms compare in the same way as for the cubic phase: the values of t-HfO_2 are about 3% smaller than those of t-ZrO_2, which are 15% smaller than of t-TiO_2. The Born effective charges of O atoms show an increasing anisotropy from t-HfO_2 to t-ZrO_2: the values of $Z^*_\perp$ for t-HfO_2 are comprised between those of t-ZrO_2, which in turn are surrounded by those of t-TiO_2. In the direction parallel to the c axis, the Born effective charges in t-HfO_2 are larger than in t-ZrO_2 by about 2% and than in t-TiO_2 by more

than 15%, showing an opposite trend with respect to the comparison for the cubic phase.

To summarize, the largest components of the Born effective charge tensors are found in r-TiO_2 and in the rutile phase in general. For the metal atoms, the strongest anisotropy is found for the Ti atoms in t-TiO_2, while for Zr and Hf atoms the strongest anisotropy appears in the rutile phase. For the oxygen atoms, the strongest anisotropy is found in r-TiO_2 and in the rutile phase in general.

2.4. Phonon Frequencies

The theoretical group analysis (see Appendix) predicts the following irreducible representations of optical and acoustical zone-center modes for the cubic phase:

$$\Gamma = \underbrace{F_{2g}}_{\text{Raman}} \oplus \underbrace{F_{1u}}_{\text{IR}} \oplus \underbrace{F_{1u}}_{\text{Acoustic}}, \tag{16}$$

for the tetragonal phase:

$$\Gamma = \underbrace{A_{1g} \oplus 2B_{1g} \oplus 3E_g}_{\text{Raman}} \oplus \underbrace{A_{2u} \oplus 2E_u}_{\text{IR}} \oplus \underbrace{A_{2u} \oplus E_u}_{\text{Acoustic}} \oplus \underbrace{B_{2u}}_{\text{Silent}}, \tag{17}$$

and for the rutile phase:

$$\Gamma = \underbrace{A_{1g} \oplus B_{1g} \oplus B_{2g} \oplus E_g}_{\text{Raman}} \oplus \underbrace{A_{2u} \oplus 3E_u}_{\text{IR}} \oplus \underbrace{A_{2u} \oplus E_u}_{\text{Acoustic}} \oplus \underbrace{A_{2g} \oplus 2B_{1u}}_{\text{Silent}}. \tag{18}$$

Although the space group differ for the tetragonal and rutile phases, their point group ($4/mmm$) is the same. Hence, the same notations appear in the irreducible representations of the zone-center modes.

Because of the non-vanishing components of the Born effective charge tensors, the dipole–dipole interaction must be properly included in the calculation of the interatomic force constants (17, 52, 53). In particular, the dipole–dipole contribution is found to be responsible for the splitting at the Γ point between the longitudinal and transverse optic (LO and TO, respectively) modes F_{1u} in the cubic phase, and E_u (perpendicular to the c axis) and A_{2u} (parallel to c axis) in the tetragonal phase.

Our calculated phonon frequencies are reported in Table 3. Our results are in very good agreement with experimental data (54–58) and previous first-principles calculations (32, 44) when available. Note that in t-TiO_2, one E_u mode has an imaginary frequency. This corresponds to a negative curvature of the total energy dependence on the atomic positions, hence to a saddle point. This vibration mode tends to break the symmetry imposed in the calculation. Hence, the tetragonal structure is found to be unstable.

Table 3. Fundamental frequencies of the cubic (c), tetragonal (t), and rutile (r) phases of HfO_2, ZrO_2 and TiO_2 (in cm^{-1}) with their symmetry assignments

	Mode		HfO_2	ZrO_2	TiO_2
c					
Raman	F_{2g}	O*	579	596	619
Infrared	F_{1u} (TO)	O	285	280	177
	F_{1u} (LO)		630	677	686
t					
Raman	A_{1g}	O*	218	259	382
	$B_{1g}(1)$	M	244	331	351
	$B_{1g}(2)$	O	582	607	669
	$E_g(1)$	M	110	147	130
	$E_g(2)$	O	479	474	435
	$E_g(3)$	O	640	659	731
Infrared	A_{2u} (TO)	O	315	339	429
	A_{2u} (LO)		621	664	678
	E_u (TO1)	O	185	153	116*i*
	E_u (LO1)		292	271	166
	E_u (TO2)	O	428	449	496
	E_u (LO2)		669	734	850
Silent	B_{2u}	O*	665	673	660
r					
Raman	A_{1g}	O*	638	626	636
	B_{1g}	O*	91	92	116
	B_{2g}	O*	792	800	844
	E_g	O*	486	483	481
Infrared	A_{2u} (TO)	O	308	301	204
	A_{2u} (LO)		670	721	779
	E_u (TO1)	O	193	197	180
	E_u (LO1)		214	274	354
	E_u (TO2)	M	222	302	404
	E_u (LO2)		296	333	448
	E_u (TO3)	O	478	462	502
	E_u (LO3)		733	765	825
Silent	A_{2g}	O*	353	368	419
	$B_{1u}(1)$	M	92	124	126
	$B_{1u}(2)$	O	428	424	423

In t-TiO_2, the E_u mode with an imaginary frequency tends to break the symmetry imposed in the calculation and implies an instability of the structure. The letter (M or O) in the second column indicates the atoms (metal or oxygen) whose motion dominates in the vibrational mode, a star superscript showing that the other atoms are fixed by symmetry.

The atomic motions associated to the various vibrational modes have been described in detail in the literature. The interested reader will refer to refs. (57, 59, 60) for the cubic and tetragonal phases, and ref. (32) for rutile.

It is very interesting to compare the phonon frequencies calculated for HfO_2, ZrO_2, and TiO_2 (see Table 3). There are several possible origins for the variations

that are observed between Hf, Zr, and Ti oxides: structural changes (e.g., the volume), change of the mass ratio Hf/Zr = 1.96 and Zr/Ti = 1.90, and differences in interatomic force constants.

The structural changes reported in Table 1 are relatively small, in particular between hafnia and zirconia. We suspect that their effect should not be the most important origin for the variations observed in the phonon frequencies. In order to check this, we compute the phonon frequencies for hafnia and titania assuming that the interatomic force constants are the same as those for zirconia, while the volume is allowed to vary. In hafnia, we find that the frequencies are decreased by at most 2%; where as in titania, they are increased by at most 6% in the cubic and tetragonal phase, and 11% in the rutile phase. This analysis shows that the structural changes play a relatively minor role in agreement with our intuition. Their effect is slightly more important in titania since the structural changes are larger (in particular in the rutile structure).

As for the role of the mass ratio, it is interesting to focus on the modes in which the M (= Hf, Zr, Ti) atoms are not much involved (either they are fixed, or they move significantly less than O atoms) and on those in which on the contrary the M (= Hf, Zr, Ti) atoms move significantly more than O atoms. In the former case (modes indicated by the letter O in the second column of Table 3), the phonon frequencies should not be affected by the change between Hf, Zr, or Ti; whereas, in the latter case (modes indicated by the letter M in the second column of Table 3), the variation should be very important.

In the cubic phase, the F_{2g} is the only mode in which the M (= Hf, Zr, Ti) atoms are fixed (as indicated by the letter O with star superscript in Table 3), and we observe indeed that the phonon frequencies do not vary very much (at most 4% with respect to zirconia). In the tetragonal phase, there are two such modes: A_{1g} and B_{2u}. While for the latter, we again do not observe any significant variation of the phonon frequencies (at most 2% with respect to zirconia); for the former, the changes are quite important: 16% decrease and 47% increase with respect to t-ZrO_2 for hafnia and titania, respectively. This is a case where the effects due to differences in the interatomic force constants are dominant. In the rutile phase, there are five modes in which the metal atoms are fixed by symmetry. Between hafnia and zirconia, the frequencies vary by at most 4% indicating that the effect of the interatomic force constants is negligible. When comparing titania to zirconia, three modes (A_{1g}, B_{2g}, and E_g) do not show significant variations, while for the other two (B_{1g} and A_{2g}) the effect of the interatomic force constants is well pronounced (25 and 14% increase of the frequencies, respectively). For the modes in which the oxygen atoms move significantly more than the metal atoms and the latter are not fixed by symmetry (as indicated by the letter O only in Table 3), the effect of the interatomic force constants is more pronounced. In particular, the mode $E_u(1)$ in the tetragonal phase even becomes unstable in titania. However, in some of these modes, this effect remains negligible (e.g., the $B_{1u}(2)$ mode in the rutile phase).

Finally, for the modes in which the M (= Hf, Zr, Ti) atoms move significantly more than O atoms (as indicated by the letter M in Table 3), it is also possible to evidence the influence of the interatomic force constants. For this purpose, we compute the phonon

frequencies for hafnia and titania assuming that the interatomic force constants are the same as those for zirconia, while the mass of the metal atom is changed to that of Hf or Ti. These simple calculations lead to frequencies which are reduced by roughly 28% for hafnia and increased by about 34% for titania with respect to zirconia. When these results compare well with those of Table 3, it can be considered that the effect of the interatomic force constants is negligible. This is actually what we find in all cases for hafnia compared to zirconia as well as for the $E_u(2)$ mode in r-TiO_2. On the contrary, the effect of the interatomic force constants is found to be very important for the B_{1g} and $E_g(1)$ modes in t-TiO_2 and for the $B_{1u}(1)$ mode in r-TiO_2.

In conclusion, while the interatomic force constants in hafnia and zirconia are very similar, they differ considerably in titania. As a result, while the differences in the phonon frequencies in Hf and Zr oxides can mostly be explained by the ratio between the masses of the two metals, the most important origin for the variation in Ti oxides is the interatomic force constants.

2.5. Dielectric Permittivity

In the cubic phase, the electronic (ϵ_∞) and static (ϵ_0) permittivity tensors are diagonal and isotropic. Due to the symmetry of the tetragonal and rutile crystals, these tensors are still diagonal, but have two independent components $\epsilon_\parallel$ and $\epsilon_\perp$, parallel and perpendicular to the c axis, respectively. In Table 4, the calculated values of ϵ_∞ and ϵ_0 are reported for the cubic, tetragonal, and rutile phases of hafnia, zirconia, and titania.

In the tetragonal phase, the ϵ_∞ tensor is only slightly anisotropic with about 5 and 10% difference between the parallel and perpendicular values for hafnia and zirconia. For titania, it is a bit more anisotropic with about 25% difference between these values. On the contrary, the ϵ_0 tensor is highly anisotropic: the value of ϵ_0 in the direction parallel to the c axis is 1.6 and 2.4 times smaller than that in the perpendicular direction for t-HfO_2 and t-ZrO_2, respectively. For t-TiO_2, the static dielectric tensor cannot be calculated due to the instability of the phase (the E_u mode with an imaginary frequency tends to break the symmetry imposed in the calculation).

In the rutile phase, the ϵ_∞ tensors present the same relatively small difference (12%) between $\epsilon_\parallel$ and $\epsilon_\perp$ for the three oxides. For hafnia and zirconia, the anisotropic character is reduced for the static dielectric permittivity tensor with 4 and 1% difference between its parallel and perpendicular components, respectively. For titania, ϵ_0 is more anisotropic than ϵ_∞.

The calculated dielectric tensors can only be compared with experimental values for the cubic and tetragonal phases of hafnia and zirconia, and for the rutile phase of titania. Moreover, a direct comparison is very difficult since there are very few data available in the literature, especially for hafnia. The main problem encountered in the experimental determination of the dielectric properties is that good quality single crystals are not available. For the tetragonal phase, the results obtained for undoped powders stabilized by their small particle size must be analyzed in the framework of effective medium theory (61). As a result, a unique value of ϵ is found without distinction between the directions parallel and perpendicular to the c axis. In order

Table 4. Electronic and static dielectric tensors for the cubic (c), tetragonal (t), and rutile (r) phases of HfO_2, ZrO_2, and TiO_2 (for t-TiO_2, the static dielectric tensor cannot be calculated due to the instability of the phase, see discussion in the text)

	HfO_2		ZrO_2		TiO_2	
c						
ϵ_∞	5.37		5.74		9.11	
$\Delta\epsilon$	20.80		27.87		128.36	
ϵ_0	26.17		33.61		137.47	
t						
	$\parallel$	$\perp$	$\parallel$	$\perp$	$\parallel$	$\perp$
ϵ_∞	5.13	5.39	5.28	5.74	6.66	8.81
$\Delta\epsilon_1$	14.87	22.34	15.03	35.48		
$\Delta\epsilon_2$		5.08		6.91		
ϵ_0	20.00	32.81	20.31	48.13		
r						
	$\parallel$	$\perp$	$\parallel$	$\perp$	$\parallel$	$\perp$
ϵ_∞	5.19	4.59	5.54	4.93	8.57	7.49
$\Delta\epsilon_1$	19.38	11.64	26.27	19.69	116.16	81.65
$\Delta\epsilon_2$		2.74		1.30		2.90
$\Delta\epsilon_3$		4.65		5.72		5.23
ϵ_0	24.58	23.62	31.81	31.64	124.74	96.28

In all the cases, the tensors are diagonal. For the cubic phase, it is also isotropic, while for the other three phases, the tensors have different components parallel ($\parallel$) and perpendicular ($\perp$) to the c axis. The contributions of the different phonon modes to the static dielectric tensor are also indicated. For the cubic phase, the contribution originates from the IR-active F_{1u} mode. For the tetragonal and rutile phases, the phonon mode contributions to $\epsilon_0^{\parallel}$ come from the IR-active A_{2u} mode, while the contributions to $\epsilon_0^{\perp}$ come from the two IR-active E_u modes.

to compare our results with experimental data, we average the values parallel and perpendicular to the c axis:

$$\bar{\epsilon} = \frac{2\epsilon_\perp + \epsilon_\parallel}{3}.$$

This average does not really have any physical meaning, and therefore the comparison is rather qualitative.

For hafnia, we are only aware of measurements of ϵ_0. Our calculated values of 26.17 for the cubic phase, and $\bar{\epsilon}_0 = 28.54$ for the tetragonal phase significantly overestimate the values of 16 (62) and 20 (63) obtained in recent measurements. This overestimation is significantly higher than what can be expected from our density functional approach and the origin of this difference remains poorly understood. For the cubic phase, our results agree within 1% with those obtained by by Zhao and Vanderbilt (43) using similar methods. However, for the tetragonal phase, our calculations disagree significantly with those of Zhao and Vanderbilt (43). In fact, we find a ratio of 1.6 between the values of the ϵ_0 tensor in directions parallel and perpendicular to the c axis, to be compared with the value of 8.6 reported by Zhao

and Vanderbilt (43). We note that the value of $\bar{\epsilon}_0 = 70$ proposed by the latter authors appears excessively high in view of the dielectric constant of the cubic phase ($\sim$26.17) and the trends observed for zirconia (see below).

For zirconia, an experimental value of $\epsilon_\infty = 4.8$ is reported in the literature for c-ZrO_2 (64,65), while measured values for t-ZrO_2 range between 4.2 (57) and 4.9 (66). Our theoretical values ($\epsilon_\infty = 5.74$ and $\bar{\epsilon}_\infty = 5.59$ for the cubic and tetragonal phases, respectively) are larger than the experimental ones by about 10–15%, as often found in the LDA to density-functional theory. For ϵ_0, the experimental values found in the literature vary from 27.2 (67) to 29.3 (68) for c-ZrO_2, and from 34.5 (67) to 39.8 (68) for t-ZrO_2. For the cubic phase, our calculated value $\epsilon_0 = 33.61$ is somewhat larger than experimental estimates, whereas, for the tetragonal phase, our calculated average $\bar{\epsilon}_0 = 38.86$ falls in the range of the experimental data.

For titania, the experimental values of the electronic permittivity tensor for the rutile phase are 6.84 and 8.43 in the directions perpendicular and parallel to the c axis (54). Our corresponding theoretical values of 7.49 and 8.57 also present the usual 10% overestimation of the LDA. For the static dielectric permittivity tensor, our theoretical values are on the same order of magnitude as the experimental results, which show quite large discrepancies: from 86 and 170 (69) to 115 and 251 (70) for the components perpendicular and parallel to the c axis, respectively.

For a deeper analysis of the static dielectric tensor, we can rely not only on the frequencies of the IR-active modes, but also on the corresponding eigendisplacements and Born effective charges. Indeed, the static dielectric tensor can be decomposed in the contributions of different modes as indicated in Eq. (13).

The contribution of the individual modes $\Delta\epsilon_\mathrm{m}$ to the static dielectric constants are presented in Table 4 (except for the t-TiO_2 phase). For each IR-active mode, the relevant component of the oscillator strength tensor is reported in Table 5. This tensor is isotropic for the F_{1u} mode in the cubic phase, while in the tetragonal and rutile phases we indicate the parallel–parallel component for the A_{2u} mode, and the perpendicular–perpendicular component for the E_u modes. We also give the magnitude of the mode-effective charge vector defined by Eq. (14) which is parallel and perpendicular to the tetragonal axis for A_{2u} and E_u modes, respectively, while it has an arbitrary orientation for the F_{1u} mode. The atomic motions for these vibrational modes have been described in detail in the literature (32, 57, 59, 60).

In Table 5, the lowest frequency modes provide the largest contributions to ϵ_0, even if their oscillator strength (S_m) is relatively small. For instance, the $E_u(1)$ mode in the tetragonal and rutile phases of hafnia and zirconia contributes much more to the static dielectric permittivity than the $E_u(2)$ mode in the tetragonal phase and the $E_u(3)$ mode in the rutile phase, which present however larger values of S_m. This emphasizes the crucial role of the frequency factor in Eq. (13). That is particularly true for the cubic phase for TiO_2 compared to ZrO_2 and HfO_2. In this case, the frequency of the F_{1u} mode in the titanium oxide is more than 35% smaller than in the other two oxides. This reduced frequency as well as the increased Born effective charge (see discussion in Section 2.3) leads to a static dielectric constant more than four times larger in c-TiO_2.

Table 5. Components of mode-effective charge vectors Z^*_m and oscillator strength tensor S_{m} for each of the IR-active modes of the cubic (c), tetragonal (t), and rutile (r) phases of HfO_2, ZrO_2, and TiO_2

	HfO_2		ZrO_2		TiO_2	
	Z^*_m	S_m	Z^*_m	S_m	Z^*_m	S_m
c						
F_{1u}	5.82	6.31	6.42	7.65	7.55	11.69
t						
A_{2u}	7.71	11.10	8.14	12.28	7.38	11.18
$E_u(1)$	5.75	5.76	5.95	5.91	6.04	6.20
$E_u(2)$	5.91	7.03	6.99	9.95	9.53	20.91
r						
A_{2u}	9.29	16.10	10.29	19.61	12.55	32.33
$E_u(1)$	4.81	3.80	6.29	6.30	9.57	17.62
$E_u(2)$	3.13	1.18	2.61	0.99	3.56	3.17
$E_u(3)$	6.18	9.31	6.39	10.09	4.88	7.12

The description of the reported vector and tensor components corresponding to the different modes is given in the text. The components of the mode-effective charge vectors are given in units of $|e|$, where e is the electronic charge. The oscillator strengths are given in 10^{-4} atomic units (1 a.u. = 253.2638413 m^3/s^2).

In the tetragonal phase of hafnia and zirconia, the same argument holds to rationalize why the ϵ_0 tensor is highly anisotropic, while the ϵ_∞ tensor is only slightly anisotropic. Indeed, in these materials, the A_{2u} has the largest oscillator strength (about twice the one of $E_u(1)$ mode) and the largest mode-effective charge. However, its frequency is about twice larger than that of the $E_u(1)$ mode, and its contribution to the static dielectric constant is thus roughly twice smaller than that of the $E_u(1)$ mode.

In Table 5, it can be observed that the oscillator strengths and the mode-effective charges essentially increase from HfO_2 to ZrO_2 and from ZrO_2 to TiO_2. This can be related to the behavior of the Born effective charges $Z^*_{\kappa,\alpha\alpha'}$ and the eigendisplacements $U_m(\kappa\alpha)$, the two quantities that appear in the definitions of $S_{m,\alpha\beta}$ and $Z^*_{m,\alpha}$ given in Eqs. (12) and (14). On the one hand, as discussed in Section 2.3, the Born effective charges show globally the following trend: $Z^*(HfO_2) \leq Z^*(ZrO_2) \leq Z^*(TiO_2)$. On the other hand, the displacements of Hf atoms are smaller than those of Zr atoms, which in turn are smaller than those of Ti atoms, simply because the mass increases from Ti to Hf (as discussed in Section 2.4).

If one now considers the contributions to the static dielectric constant reported in Table 4, it appears clearly that $\Delta\epsilon(HfO_2) \leq \Delta\epsilon(ZrO_2) \leq \Delta\epsilon(TiO_2)$ for almost of all the modes. For a few modes, however, despite the fact that the oscillator strengths are smaller, the corresponding contribution presents exactly the opposite trend due to an increase of the corresponding phonon frequencies. For instance, for $E_u(3)$ mode in the rutile phase, the frequency for ZrO_2 is much smaller than for TiO_2. As a result, the increase by 220% of the oscillator strengths is completely compensated by the

raise of 34% in the frequency: in the end, the contribution for TiO_2 is 9% larger than the one for ZrO_2.

3. CRYSTALLINE SILICATES

3.1. Introduction

Due to the chemical homology of Hf and Zr discussed in Section 2.1, hafnon ($HfSiO_4$) and zircon ($ZrSiO_4$) resemble each other in many physical and chemical properties. Their similarities are such that there is complete miscibility between hafnon and zircon (71). In addition to their importance as potential alternative gate dielectrics, hafnon and zircon are of geological significance. They both belong to the orthosilicate class of minerals, which can be found in igneous rocks and sediments. Zircon is used as a gemstone, because of its good optical quality, and resistance to chemical attack. In the earth's crust, hafnon and zircon are host minerals for the radioactive elements uranium and thorium. They have therefore widely been studied in the framework of nuclear waste storage.

In a recent paper (72), we have studied the structural, electronic and dynamical properties of zircon using first-principles calculations. In this section, we present a comparison between the naturally occurring $ZrSiO_4$ and $HfSiO_4$ crystals, and we also consider the $TiSiO_4$ crystal defined by similarity with hafnon and zircon. By lexical analogy, we will also refer to this hypothetical structure as titanon.

3.2. Structural Properties

The $MSiO_4$ with M (= Hf, Zr, Ti) crystals, which are represented in Fig. 2, have a conventional unit cell which is body-centered tetragonal (space group $I4_1/amd$, N° 141) and contains four formula units of $MSiO_4$, as illustrated by the dashed lines in Fig. 2(b). A primitive cell containing only two formula units of $MSiO_4$ can also be defined, as indicated by the heavy lines in Fig. 2(b).

The structure of hafnon, zircon, and titanon crystals may be viewed as consisting of $(SiO_4)^{4-}$ anions and M^{4+} cations with M (= Hf, Zr, Ti), as illustrated by the medium grey tetrahedra and the light grey spheres in Fig. 2(b). This is consistent with the larger bond length (about 25%) of the M–O compared to the Si–O bond.

Alternatively, as presented in Fig. 2(c), a different view may be adopted in which $HfSiO_4$, $ZrSiO_4$, and $TiSiO_4$ consist of alternating (discrete) SiO_4 tetrahedra and MO_8 units, sharing edges to form chains parallel to the c-direction. Note that in these MO_8 units four O atoms are closer to the M atom than the four other ones (about 6, 6, and 11% difference in the M–O bond length in hafnon, zircon, and titanon, as reported in Table 6).

The positions of the M (= Hf, Zr, Ti) and Si atoms are imposed by symmetry: they are located at $(0, \frac{3}{4}, \frac{1}{8})$ and $(0, \frac{1}{4}, \frac{3}{8})$ on the 4a and 4b Wyckoff sites, respectively. The O atoms occupy the 16h Wyckoff sites $(0, u, v)$, where u and v are internal parameters.

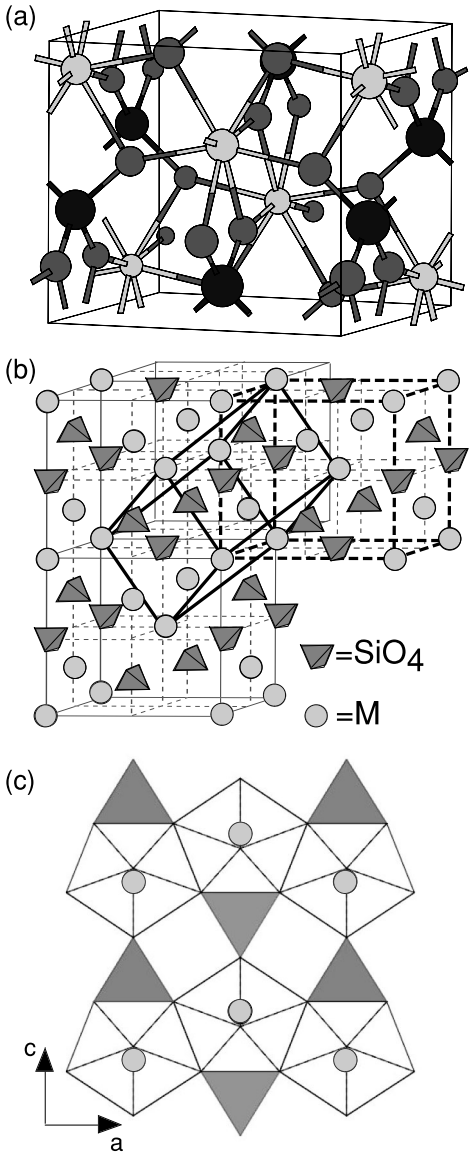

Fig. 2. Structure of $HfSiO_4$, $ZrSiO_4$, and $TiSiO_4$. (a) A ball and stick representation is adopted for the body-centered-tetragonal unit cell, where the M (= Hf, Zr, Ti), O, and Si atoms are colored in light, medium, and dark grey respectively. (b) The individual SiO_4 units are represented schematically by the medium grey tetrahedra, while M atoms are indicated by light grey spheres. The two sets of dashed lines and heavy lines outline the body-centered-tetragonal unit cell and the primitive cell, respectively. (c) Besides the SiO_4 units, the MO_8 triangular dodecahedra with the M atoms in their center are also drawn.

Table 6. Structural parameters of $HfSiO_4$, $ZrSiO_4$, and $TiSiO_4$

	$HfSiO_4$		$ZrSiO_4$		$TiSiO_4$
	Th.	Expt.	Th.	Expt.	Th.
a	6.61	6.57	6.54	6.61	6.21
c	5.97	5.96	5.92	6.00	5.81
u	0.0672	0.0655	0.0645	0.0646	0.0591
v	0.1964	0.1948	0.1945	0.1967	0.1892
Volume	130.42	128.63	126.60	131.08	112.03
d(Si–O)	1.62	1.61	1.61	1.62	1.60
d(M–O)	2.14	2.10	2.10	2.13	1.95
	2.27	2.24	2.24	2.27	2.19
∠(O-Si-O)	97°	97°	97°	97°	96°
	116°	117°	116°	116°	117°

The lengths are expressed in Å. The experimental data are taken from Speer and Cooper (71) for $HfSiO_4$, and from Mursic et al. (73) for $ZrSiO_4$.

Table 6 summarizes our results obtained after structural and atomic relaxation. The calculated lattice constants a and c, as well as the internal parameters u and v are found to be in excellent agreement with their corresponding experimental values for hafnon (71) and zircon (73). Interatomic distances and angles are within 1 or 2% of the experimental values. This accuracy is to address in a meaningful way the dynamical and dielectric properties.

The structural parameters for Hf- and Zr-based silicates are very close, whereas those for Ti-based materials can be 5–10% larger than for the two other silicates. The largest difference is found for the shorter Ti–O bond which is 9 and 10% smaller than the Zr–O and Hf–O distances, respectively. This is further confirmation of the different chemistry of 3d metals with respect to 4d and 5d metals.

3.3. Electronic Structure

In Fig. 3, we present the calculated electronic density of states (DOS) for hafnon, zircon, and titanon. The complete electronic band structure for $ZrSiO_4$ along several directions in the Brillouin zone can be found elsewhere (72). For $HfSiO_4$ and $TiSiO_4$, the electronic band structure is very similar apart from the position of the Hf 5s and 5p bands in hafnon and the Ti 3s and 3p bands in titanon, as explained hereafter.

We clearly distinguish four groups in the DOS of the valence bands, of which the three lowest ones are rather peaked (small dispersion of the bands), indicative of a weak hybridization. The DOS of hafnon, zircon, and titanon exhibit a very sharp peak at −60.2, −47.1, and −56.5 eV, respectively, which are attributed to the Hf 5s, Zr 4s, Ti 3s states, respectively. Each of these peaks corresponds to two flat bands in the band structure (72). The peaks at −29.8 eV for hafnon, −25.5 eV for zircon, and −33.1 eV for titanon are related to the Hf 5p, Zr 4p, and Ti 3s states, respectively. Each of these peak includes six electrons per unit cell. Finally, the O 2s peak (8 electrons per unit cell) is located between −18.0 and −16 eV for hafnon, zircon, and titanon.

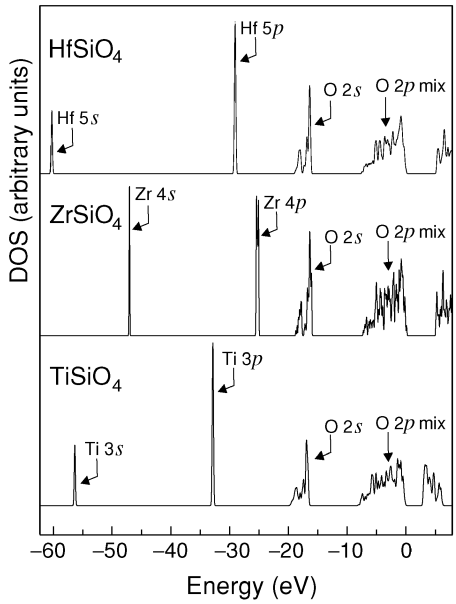

Fig. 3. Electronic density of states (DOS) for $HfSiO_4$, $ZrSiO_4$, and $TiSiO_4$.

By contrast, the fourth group (24 electrons per unit cell), has a much wider spread of 8 eV. These states have mainly an O 2p character with some mixing of Si and M (= Hf, Zr, Ti) orbitals. This mixed covalent–ionic bonding of $HfSiO_4$ and $ZrSiO_4$, appearing in this group of valence bands, should be kept in mind when interpreting the Born effective charge tensors.

3.4. Born Effective Charge Tensors

In the hafnon, zircon, and titanon structures, the local site symmetry of M (= Hf, Zr, Ti) and Si atoms is rather high ($\bar{4}m2$). The Born effective charge tensors of M (= Hf, Zr, Ti) and Si atoms are diagonal and have only two independent components: parallel and perpendicular to the tetragonal axis, $Z^*_{\parallel}$ and $Z^*_{\perp}$, respectively. The Born effective charge tensors of M (= Hf, Zr, Ti) and Si atoms are reported in Table 7.

We note that $Z^*_{\perp}$ for M (= Hf, Zr, Ti) is anomalously large compared to the nominal ionic charge of the hafnium, zirconium, titanium ions $Z = +4$. A similar behavior was also observed in the case of $PbZrO_3$ (49) and of hafnia and zirconia, as discussed in Section 2. A detailed analysis of the physics of Born effective charges in the case of perovskite ferroelectrics (like $PbZrO_3$) ascribed this effect to a mixed covalent–ionic bonding (50). In Section 3.3, we have seen the occurrence of M–O 2p hybridization. Thus the physical interpretation of this phenomenon is likely similar to the case of perovskite ferroelectrics. The other component of the M (= Hf, Zr, Ti) Born effective charge tensor ($Z^*_{\parallel}$) is also larger than the nominal ionic charge, although the effect is not as pronounced (in the case of Ti, it is basically equal to the nominal charge).

Table 7. Non-vanishing components of the calculated Born effective charge tensors for M (= Hf, Zr, Ti), Si, and O atoms in $HfSiO_4$, $ZrSiO_4$, and $TiSiO_4$.

Atom	$HfSiO_4$	$ZrSiO_4$	$TiSiO_4$
M	$(+5.28\ +5.28\ +4.68)$	$(+5.41\ +5.41\ +4.63)$	$(+5.91\ +5.91\ +4.01)$
Si	$(+3.18\ +3.18\ +4.35)$	$(+3.25\ +3.25\ +4.42)$	$(+3.56\ +3.56\ +4.83)$
O[a]	$\begin{pmatrix} -1.15 & 0 & 0 \\ 0 & -3.08 & -0.19 \\ 0 & -0.35 & -2.26 \end{pmatrix}$	$\begin{pmatrix} -1.15 & 0 & 0 \\ 0 & -3.17 & -0.16 \\ 0 & -0.34 & -2.25 \end{pmatrix}$	$\begin{pmatrix} -1.20 & 0 & 0 \\ 0 & -3.54 & -0.11 \\ 0 & -0.45 & -2.22 \end{pmatrix}$
	$[-1.15\ -3.16\ -2.18]$	$[-1.15\ -3.23\ -2.19]$	$[-1.20\ -3.58\ -2.18]$

For M (= Hf, Zr, Ti) and Si atoms, the tensors are diagonal and only the principal elements are given. For O atoms, the full tensor is reported and the principal elements of its symmetric part are indicated between brackets.

[a] The tensors reported in the table for O atoms refer to the atom located at (0, u, v). The Born effective charge tensors for the other oxygen atoms can be obtained using the symmetry operations.

For the silicon atom, there are also some (weaker) deviations with respect to the nominal value ($Z = +4$), one component being larger, and one being lower. While for hafnon and zircon, the deviations are the largest for the perpendicular components; for titanon, it is the parallel component that differs the most from the nominal charge. These deviations are not very different from those observed in tetrahedrally bonded silica polymorphs, like quartz (74), in which each O atom is strongly bonded to two Si atoms, or in the more compact polymorph of silica, stishovite (51), in which each O atom has three close Si neighbors.

Note that $Z^*_\perp$ is about 3% smaller for hafnium in $HfSiO_4$ than for zirconium in $ZrSiO_4$, which in turn is about 10% smaller than for titanium in $TiSiO_4$. This is very similar to what is observed in hafnia, zirconia, and titania as discussed in Section 2.3. The Born effective charge of Si atoms for directions perpendicular to the tetragonal axis shows a very similar behavior: it is about 2% smaller in hafnon than in zircon, and 10% smaller in the latter than in titanon. For the Born effective charge in a direction parallel to the c axis, we find for Si atoms the same trend as for perpendicular directions, but the opposite one for M (= Hf, Zr, Ti) atoms: the Born effective charges for Hf in hafnon is about 1% higher than for Zr in zircon, which in turn is about 15% higher than for Ti in titanon.

The local site symmetry of the O atoms has only a mirror plane. As a consequence, the Born effective charge tensors of O atoms are not diagonal, and depend on five independent quantities. We examine the tensor for the O atom located at (0, u, v), which is reported in Table 7. The Born effective charge tensors of the other oxygen atoms can be obtained using the symmetry operations. For this particular atom, the mirror plane is perpendicular to x. Note that Z^*_{yz} and Z^*_{zy} are different, but rather small, making the Born effective charge tensor almost diagonal. They appear in the mirror plane, where one O–Si bond and two O–M bonds (one long and one short) are present. One can compute the projection of the Born effective charge on these

directions. For the O–Si bond, the projection is −3.00 in $HfSiO_4$ −3.01 in $ZrSiO_4$, and −3.22 in $TiSiO_4$. For the O–M bonds, the projections on the shorter and longer ones are −3.15 and −2.25 in hafnon, −3.23 and −2.29 in zircon, and −3.60 and −2.36 for titanon, respectively. In this plane, the magnitude of the Born effective charge components is larger than the nominal ionic charge of oxygen ($Z = -2$). Following an alternative approach to the characterization of the anisotropy of this tensor, we select its symmetric part and diagonalize it. The principal values are given in Table 7 and the principal direction associated to the largest principal value forms an angle of about 20° with respect to the y axis. Both analyses give the same type of anisotropy.

Such a strong anisotropy of the Born effective charge tensor for O atoms, with one component of magnitude much smaller than 2 and much smaller than the two others, was already observed in SiO_2-stishovite (51). By contrast, in tetrahedrally bonded silica, there are *two* components of magnitudes much smaller than 2. Thus, at the level of the Born effective charges, the ionic-covalent bonding of O atoms to M (= Hf, Zr, Ti) and Si atoms in $HfSiO_4$, $ZrSiO_4$, and $TiSiO_4$ is closer to stishovite than to quartz, in agreement with a naive bond-counting argument. Models of amorphous silicates MSi_xO_y should take into account this difference, and might be classified according to the anisotropy of the O Born effective charges. One expects that, for a small content of M (= Hf, Zr, Ti), the quartz-like behavior dominates, while, for M atomic fractions closer to that of hafnon, zircon, and titanon, the stishovite-like behavior becomes stronger.

Note finally that the Born effective charges for O atoms are very similar in $HfSiO_4$, $ZrSiO_4$, and $TiSiO_4$. The first principal component is the same in $HfSiO_4$ and $ZrSiO_4$, while it is 4% larger (in absolute value) in $TiSiO_4$. The last principal component is basically the same for all three silicates. The only significant difference is for the second principal value, which is 2% smaller in hafnon and 13% in titanon with respect to zircon.

3.5. Phonon Frequencies

We also compute the phonon frequencies at the Γ point of the Brillouin zone for hafnon and zircon. The theoretical group analysis (see Appendix) predicts the following irreducible representations of optical and acoustical zone-center modes:

$$\Gamma = \underbrace{2A_{1g} \oplus 4B_{1g} \oplus B_{2g} \oplus 5E_g}_{\text{Raman}} \oplus \underbrace{3A_{2u} \oplus 4E_u}_{\text{IR}} \oplus \underbrace{A_{2u} \oplus E_u}_{\text{Acoustic}} \oplus \underbrace{B_{1u} \oplus A_{2g} \oplus A_{1u} \oplus 2B_{2u}}_{\text{Silent}}.$$

Because of the non-vanishing components of the Born effective charge tensors, the dipole–dipole interaction must be properly included in the calculation of the interatomic force constants (17, 52, 53). In particular, the dipole–dipole contribution is found to be responsible for the splitting between the longitudinal and transverse optic (LO and TO, respectively) modes E_u (perpendicular to c) and A_{2u} (parallel to c) at the Γ point.

Table 8. Fundamental frequencies of $HfSiO_4$, $ZrSiO_4$, and $TiSiO_4$ (in cm^{-1}) with their symmetry assignments

			$HfSiO_4$		$ZrSiO_4$		$TiSiO_4$
	Mode		Th.	Expt.	Th.	Expt.	Th.
Raman	$A_{1g}(1)$	O*	462	450	442	439	383
	$A_{1g}(2)$	O*	970	984	971	974	1011
	$B_{1g}(1)$	M	162	157	225	214	259
	$B_{1g}(2)$	O	395	401	397	393	418
	$B_{1g}(3)$	O	638	620	632	–	627
	$B_{1g}(4)$	O	1016	1020	1017	1008	1047
	B_{2g}	O*	247	267	252	266	263
	$E_g(1)$		161	148	194	201	194
	$E_g(2)$		204	212	225	225	242
	$E_g(3)$		369	351	375	357	430
	$E_g(4)$	O	530	–	536	547	544
	$E_g(5)$	O	923	–	923	–	319
Infrared	A_{2u}(TO1)		312		348	338	319
	A_{2u}(LO1)		423		476	480	482
	A_{2u}(TO2)	O	598		601	608	606
	A_{2u}(LO2)		656		646	647	631
	A_{2u}(TO3)	O	983		980	989	1000
	A_{2u}(LO3)		1095		1096	1108	1106
	E_u(TO1)		252		285	287	303
	E_u(LO1)		313		341	352	374
	E_u(TO2)	O	395		383	389	374
	E_u(LO2)		409		420	419	414
	E_u(TO3)	O	420		422	430	433
	E_u(LO3)		461		466	471	497
	E_u(TO4)	O	873		867	885	877
	E_u(LO4)		1023		1029	1035	1048
Silent	B_{1u}	O*	107		120		125
	A_{2g}	O*	233		242		250
	A_{1u}	O*	383		392		418
	$B_{2u}(1)$	O*	573		566		547
	$B_{2u}(2)$	O*	945		943		969

The letter (M or O) in the second column indicates the atoms (metal or oxygen) whose motion dominates in the vibrational mode, a star superscript showing that the other atoms are fixed by symmetry. The experimental values are taken from Hoskin and Rodgers (76) for $HfSiO_4$ (Raman modes only), and from Dawson et al. (77) for $ZrSiO_4$.

The calculated phonon frequencies are reported in Table 8. Our results are in excellent agreement with the values reported in experiments for hafnon (75, 76), and for zircon (77–79), with a rms absolute deviation of 4.1 cm^{-1} for $HfSiO_4$ (9.4 cm^{-1} for $ZrSiO_4$), and a rms relative deviation of 4.2% (2.5%).

In Section 2.4, we have pointed out three origins for the variations of the frequencies in Hf and Zr based oxides: the structural changes, the mass ratio equal to 1.96

for Hf/Zr and 1.90 for Zr/Ti, and the differences in interatomic force constants. It is quite interesting to compare on the same basis the phonon frequencies calculated for $HfSiO_4$, $ZrSiO_4$, and $TiSiO_4$ (see Table 8).

By performing a similar analysis as for the oxides, we find that the structural changes play a very minor role, in agreement with the intuition resulting from the very small variations observed in Table 6. With respect to zircon, we find that the frequencies in hafnon are decreased by about 1%; where as in titanon, they are increased by at most 6%.

As for the oxides, the mass ratio should play a major role for the modes in which the M (= Hf, Zr, Ti) atoms move significantly more than O atoms (as indicated by the letter M in the second column of Table 8). This is the case for the $B_{1g}(1)$ mode. The effect of the mass ratio on the phonon frequencies can be roughly estimated by assuming that the interatomic force constants for hafnon and titanon are the same as those for zircon, while the mass of the metal atom is changed to that of Hf or Ti. These simple calculations lead to frequencies which are reduced by roughly 28% for hafnon and increased by about 33% for titanon with respect to zircon. In Table 8, we observe that, for hafnon, the estimation above is very good; while, for titanon, the frequency only increases by 15% indicating an important change in the interatomic force constants.

On the contrary, the frequencies should not vary much between the three silicates for modes in which the M (= Hf, Zr, Ti) atoms are fixed by symmetry as indicated by the letter O with a star superscript in Table 8, as well as for those in which the O atoms move significantly more than the M (= Hf, Zr, Ti) atoms (as indicated by the letter O). In most of these cases, this is indeed what is observed; in a few cases, however, the differences in the interatomic force constants dominate (for instance, for the $A_{1g}(1)$ mode in $TiSiO_4$ or the B_{1u} mode in $HfSiO_4$ for which the frequencies decrease by 11 and 14% with respect to $ZrSiO_4$.

In summary, the effect of the interatomic force constants is less pronounced for the silicates than for the oxides. As a result, the differences in the phonon frequencies in Hf, Zr, and Ti silicates can mostly be explained by the ratio between the masses of the three metals.

3.6. Dielectric Permittivity

Due to the tetragonal symmetry of the hafnon, zircon, and titanon crystals, the electronic (ϵ_∞) and static (ϵ_0) permittivity tensors have two independent components $\epsilon_\parallel$ and $\epsilon_\perp$ parallel and perpendicular to the c axis, respectively. The calculated values of ϵ_∞ and ϵ_0 are reported in Table 9.

For zircon, values of 10.69 (3.8) (78) and 11.25 (3.5) (79) are reported for the static (electronic) dielectric permittivity in the directions parallel and perpendicular to the tetragonal axis, respectively. Our theoretical values are larger than the experimental ones by about 10%, as often found in the LDA to density functional theory. For hafnon, we were not able to find accurate measurements in the literature: for hafnium silicates, values ranging from 11 to 25 have been reported.

Table 9. Electronic and static dielectric tensors of $HfSiO_4$, $ZrSiO_4$, and $TiSiO_4$

	$HfSiO_4$		$ZrSiO_4$		$TiSiO_4$	
	$\parallel$	$\perp$	$\parallel$	$\perp$	$\parallel$	$\perp$
ϵ_∞	4.11	3.88	4.26	4.06	5.52	5.56
$\Delta\epsilon_1$	4.93	4.38	5.90	5.16	9.90	11.54
$\Delta\epsilon_2$	0.81	0.75	0.52	1.31	0.31	0.00
$\Delta\epsilon_3$	0.80	0.35	0.85	0.05	1.01	0.46
$\Delta\epsilon_4$		1.27		1.38		1.88
ϵ_0	10.65	10.63	11.53	11.96	16.73	19.44

The contributions of individual phonon modes to the static dielectric tensor are indicated. The tensors are diagonal and have different components parallel ($\parallel$) and perpendicular ($\perp$) to the c axis. The phonon mode contributions to $\epsilon_0^{\parallel}$ come from the three IR-active A_{2u} modes, while the contributions to $\epsilon_0^{\perp}$ come from the four IR-active E_u modes.

The contribution of the individual modes $\Delta\epsilon_{\mathrm{m}}$ to the static dielectric constant, as defined in Eq. (13), are also indicated in Table 9. The largest contribution comes from the lowest frequency mode. The decomposition of the static dielectric tensor can further be analyzed using the mode-effective charge vectors and the oscillator strength tensors, defined by Eqs. (14) and (12), respectively. In Table 10, we present for each IR-active mode, the magnitude of its mode-effective charge vectors (this vector is parallel and perpendicular to the tetragonal axis for A_{2u} and E_u modes, respectively), as well as the relevant component of the oscillator strength tensor (the parallel–parallel component for A_{2u} modes, and the perpendicular–perpendicular component for E_u modes).

Table 10. Components of mode-effective charge vectors Z^*_{m} and oscillator strength tensor S_{m} for each of the IR-active modes for $HfSiO_4$, $ZrSiO_4$, and $TiSiO_4$

	$HfSiO_4$		$ZrSiO_4$		$TiSiO_4$	
	Z^*_m	S_m	Z^*_m	S_m	Z^*_m	S_m
$A_{2u}(1)$	6.85	7.39	7.68	10.06	7.73	12.53
$A_{2u}(2)$	3.78	4.24	2.76	2.64	2.05	1.41
$A_{2u}(3)$	6.60	11.22	6.71	11.50	7.10	12.49
$E_u(1)$	5.93	4.05	6.79	5.91	8.45	13.22
$E_u(2)$	2.94	1.70	3.51	2.71	0.90	0.00
$E_u(3)$	1.69	0.91	0.28	0.12	2.66	1.08
$E_u(4)$	7.21	14.02	7.37	14.69	8.10	18.05

The description of the reported vector and tensor components corresponding to the two types of modes is given in the text. The components of the mode-effective charge vectors are given in units of $|e|$, where e is the electronic charge. The oscillator strengths are given in 10^{-4} atomic unit (1 a.u. = 253.2638413 m^3/s^2).

For each symmetry representation (A_{2u} and E_u), the lowest and highest frequency modes exhibit the largest mode effective charges and the largest oscillator strengths. Despite their similar oscillator strengths, the modes of lowest frequency contribute much more to the static dielectric constant than the modes of highest frequency, the frequency factor in Eq. (13) playing a crucial role. The other modes contribute significantly less to the static dielectric constants.

For the lowest and highest frequency modes, the oscillator strengths and the mode-effective charges increase from hafnon to zircon and from zircon to titanon. The origin of this difference can be traced back to the Born effective charges and the eigendisplacements. Indeed, as discussed in Section 3.4, the Born effective charges of M (= Hf, Zr, Ti) and Si atoms show the following behavior: $Z^*(HfOSi_4) \leq Z^*(ZrSiO_4) \leq Z^*(TiSiO_4)$. Moreover, due to their heavier weight, the displacements of Hf atoms are smaller than those of Zr atoms, which in turn are smaller than those of Ti atoms.

Coming back to the contributions to the static dielectric constant reported in Table 9, we observe that the contributions of the lowest and highest frequency modes show the following increasing trend: $\Delta\epsilon(HfSiO_4) \leq \Delta\epsilon(ZrSiO_4) \leq \Delta\epsilon(TiSiO_4)$. This behavior is essentially related to the increase in the oscillator strengths, since the phonon frequencies do not change significantly in all three silicates.

4. AMORPHOUS SILICATES

The dielectric properties of transition metal amorphous silicates constitute an issue of great practical importance. Early experimental measurements tend to show a supralinear dependence of the static dielectric constant ϵ_0 on the metal concentration (6, 7). While several phenomenological theories address this behavior (80, 81), a close to linear dependence seem to prevail based on more recent (82, 83). In a recent paper (84), we have used DFT simulations to tackle this particularly relevant problem by analyzing how the permittivity of Zr silicates is affected by the underlying microscopic structure.

In addressing this technological issue, we face the more general problem of predicting the dielectric properties of amorphous alloys using first-principles calculations. Brute force investigation of numerous large supercells is beyond present computational capabilities. To overcome this difficulty, we explore the relationship between the dielectric properties of Zr silicates and their underlying microscopic structure. Using density-functional theory, we determine optical and static dielectric constants for various model structures of Zr silicates, both ordered and disordered. We introduce a scheme which relates the dielectric constants to the local bonding of Si and Zr atoms. This scheme relies on the definition of parameters characteristic of the basic structural units (SUs) formed by Si and Zr atoms and their nearest neighbors.

Applied to amorphous Zr silicates, our scheme provides a good description of measured dielectric constants, both optical (83, 85) and static (82, 83), and shows the important contribution of ZrO_6 SUs to the static dielectric constant. In a very similar

way, our scheme can also be used to investigate Hf and Ti silicates. We here only briefly indicate how these systems compare with each other.

We set up a series of model structures of $(ZrO_2)_x(SiO_2)_{1-x}$ with x ranging from 0 to 0.5, nine crystalline and one amorphous, and describe them in terms of cation-centered SUs. We start with three different SiO_2 polymorphs ($x = 0$):

- C_0: α-cristobalite with four SiO_4 SUs per unit cell
- Q_0: α-quartz with three SiO_4 SUs
- S_0: stishovite with two SiO_6 SUs

We derive three new crystal structures by replacing one of the Si atoms by a Zr atom for each of these models:

- C_1: Zr^{Si} in α-cristobalite with three SiO_4 and one ZrO_4 SUs per unit cell ($x = 0.25$)
- Q_1: Zr^{Si} in α-quartz with two SiO_4 and one ZrO_4 SUs ($x = 0.33$)
- S_1: Zr^{Si} in stishovite with one SiO_6 and one ZrO_6 SUs

We also consider the zircon crystal, as well as two other models generated by substituting Zr by Si:

- Z_2: zircon which contains two SiO_4 and two ZrO_8 SUs per unit cell ($x = 0.5$)
- Z_1: Si^{Zr} in zircon with two SiO_4, one SiO_6, and one ZrO_8 SUs ($x = 0.25$)
- Z_0: fully Si-substituted zircon with two SiO_4 and SiO_6 SUs ($x = 0$)

Finally, only a single disordered structure could be afforded because of the noticeable computational cost associated:

- A: amorphous structure, generated using classical molecular dynamics with empirical potentials (84), with 3 ZrO_4 and 17 SiO_4 SUs ($x = 0.15$)

The atomic coordinates and the cell parameters of all our model structures are fully relaxed within the local density approximation (LDA) to DFT. The calculated optical and static dielectric constants for our model structures are given in Table 11. Due to the well-known limitations of the LDA, the theoretical values are larger than the experimental ones (when available) by about 10%.

In order to analyze the dependence of the optical dielectric constant (ϵ_∞) on the underlying atomic nanostructure, we use the Clausius–Mosotti relation (81, 83) that connects it to the electronic polarizability $\bar{\alpha}$:

$$\frac{\epsilon_\infty - 1}{\epsilon_\infty + 2} = \frac{4\pi}{3}\frac{\bar{\alpha}}{\bar{V}}, \tag{19}$$

where $\bar{V}$ is the average SU volume. The polarizability $\bar{\alpha}$ can be considered as a local and additive quantity, in contrast with ϵ_∞. Hence, we define α_i values for each SU i, where $i \equiv SiO_n$ (with $n = 4$ or 6) or ZrO_n (with $n = 4$, 6, or 8), in such a way that:

$$\bar{\alpha} = \sum_i x_i \alpha_i, \tag{20}$$

Table 11. Composition (x), optical (ϵ_∞) and static (ϵ_0) dielectric constants, volume ($\bar{V}$) in bohr^3, polarizability $\bar{\alpha}$ in bohr^3, characteristic dynamical charge ($\bar{Z}$), and characteristic force constant ($\bar{C}$) in hartree/bohr^2 for the various model systems

Model	x	ϵ_∞	ϵ_0	$\bar{V}$	$\bar{\alpha}$	$\bar{Z}$	$\bar{C}$
C_0	0.00	2.38	4.30	264.77	19.92	4.21	0.4391
C_1	0.25	2.76	5.25	273.21	24.12	4.59	0.3895
Q_0	0.00	2.54	4.83	240.34	19.46	4.28	0.4169
Q_1	0.33	2.91	5.84	275.28	25.56	4.85	0.3661
S_0	0.00	3.36	10.33	153.74	16.16	4.81	0.2716
S_1	0.50	4.44	24.20	201.88	25.74	6.14	0.1188
Z_0	0.00	3.37	10.11	167.80	17.68	4.76	0.2512
Z_1	0.25	3.94	18.36	189.74	22.42	5.29	0.1287
Z_2	0.50	4.13	11.81	213.28	26.00	5.58	0.2385
A	0.15	3.24	8.92	213.12	21.75	4.83	0.2424

The reported dielectric constants correspond to orientational averages.

where x_i is the molecular fraction. In Table 12, we report the five α_i values that we determine by solving in a least square sense the overdetermined system based on the calculations of ϵ_∞ for the nine crystalline models. The optical dielectric constants derived from these α_i values using Eqs. (19) and (20) are in very good agreement with those computed from first-principles, showing average and maximal errors smaller than 1 and 2.5%, respectively. For the amorphous model, which was not used to determine the α_i values, the calculated value $\epsilon_\infty = 3.25$ compares very well with the first-principles result $\epsilon_\infty = 3.24$. These results give an *a posteriori* motivation for the use of Eqs. (19) and (20) to model the optical dielectric constant.

For the static dielectric constant (ϵ_0), the description in terms of a single local and additive quantity as the electronic polarizability is precluded by the phonon contributions. To overcome this difficulty, we consider the difference between dielectric constants ($\Delta\epsilon$):

$$\Delta\epsilon = \epsilon_0 - \epsilon_\infty = \frac{4\pi}{\Omega_0} \sum_m \frac{S_m}{\omega_m^2} = \frac{4\pi}{\bar{V}} \frac{\bar{Z}^2}{\bar{C}}, \tag{21}$$

Table 12. Polarizability (α in bohr^3), characteristic dynamical charge (Z), and characteristic force constant (C in hartree/bohr^2) for various structural units, extracted from the calculations for the nine crystalline models

	SiO_4	SiO_6	ZrO_4	ZrO_6	ZrO_8
α	19.68	16.14	37.37	35.35	32.69
Z	4.29	4.92	5.66	7.16	6.73
C	0.3597	0.2176	0.4202	0.0817	0.1153

where ω_m and S_m are the frequency and the oscillator strength of the mth mode. The volume of the primitive unit cell Ω_0 is related to the volume $\bar{V}$ and to the number of SUs $\bar{N}$ by $\Omega_0 = \bar{N}\bar{V}$. The characteristic dynamical charge $\bar{Z}$ and characteristic force constant $\bar{C}$ are defined by:

$$\bar{Z}^2 = \frac{1}{\bar{N}} \sum_{\kappa} Z_{\kappa}^2 \quad \text{and} \quad \bar{C}^{-1} = \frac{1}{\bar{N}} \sum_{m} \frac{S_m}{\omega_m^2 \bar{Z}^2}, \tag{22}$$

where Z_κ are the atomic Born effective charges.

A detailed analysis of the variation of $\Delta\epsilon$ due to a Si $\rightarrow$ Zr substitution is given in ref. (84), where the contribution from sixfold coordinated atoms has been highlighted. In fact, these configurations are very similar to those in ABO_3 perovskites. The enhancement of $\Delta\epsilon$ finds its origin in very low frequency modes in which the cations (A or B) move in opposition with the O atoms while carrying opposite effective charges.

By analogy with the polarizability, we define Z_i and C_i values for each SU such that:

$$\bar{Z}^2 = \sum_i x_i Z_i^2 \quad \text{and} \quad \bar{C}^{-1} = \sum_i x_i C_i^{-1}, \tag{23}$$

though the locality and the additivity of these parameters is not guaranteed *a priori*. We determine the optimal values Z_i and C_i in the same way as for α_i (Table 12).

For the nine crystalline models, the values of $\Delta\epsilon$ obtained by introducing these parameters in Eqs. (21) and (23) match quite well those calculated from first-principles (84), though the agreement is not as impressive as for ϵ_∞. Differences result primarily from the determination of $\bar{C}$. By contrast, the values of $\bar{Z}$ given by Eq. (23) agree very well with those computed from first principles, showing an average and maximal error smaller than 2 and 3%, respectively. *A posteriori*, $\bar{C}$ appears to be less local and additive. In fact, it can be demonstrated that the locality of $\bar{C}$ is closely related to the dynamical charge neutrality of the SUs (84).

For the amorphous model, which was not used to determine the Z_i and C_i values, the agreement between the model and the first-principles $\Delta\epsilon$ is excellent with an error smaller than 1% (84). Indeed, our scheme is more accurate for disordered systems, where the localization of vibrational modes is enhanced and the dynamical charge neutrality appears better respected.

The parameters in Table 12 fully determine the dielectric constants of Zr silicates of known composition in terms of SUs. It is important to note the following two points. On the one hand, the three parameters of Zr-centered SUs all contribute to enhancing the dielectric constants over those of Si-centered ones of corresponding coordination.[1] This is clearly at the origin of the increase of ϵ_∞ and ϵ_0 with increasing Zr concentration. Second, while the polarizability α_i of a given SU (Si- or Zr-centered) steadily decreases with increasing coordination, such a regular behavior is not

[1] In Table 12, the value of C for SiO_4 apparently leads to a higher contribution to $\Delta\epsilon$ than that for ZrO_4. This is an artifact of the approach we used to determine the Z_i and C_i.

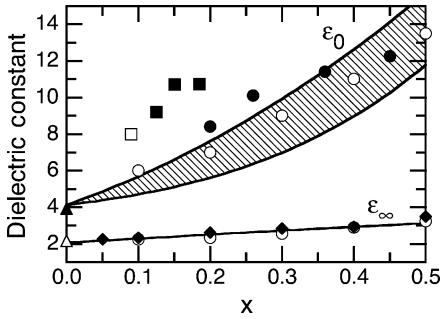

Fig. 4. Dielectric constants (ϵ_∞ and ϵ_0) as a function of composition x for amorphous $(ZrO_2)_x(SiO_2)_{1-x}$. The hatched region corresponds to results derived from our model scheme and reflects the indetermination of the number of ZrO_6 units. The upper curve delimiting the band corresponds to structures entirely composed of ZrO_6 units, while the lower curve represents a smooth transition from a structure composed of ZrO_4 units at $x = 0$ to one composed of ZrO_8 units at $x = 0.5$, without the occurrence of any ZrO_6 unit. The references for the experimental data are: ♦ (85), ● (82), ○ (83), ■ (6, 7), □ (86), ▲ (87), and △ (30).

observed for the parameters Z_i and C_i determining $\Delta\epsilon$. On the other hand , Z_i and C_i concurrently vary to enhance the contribution of ZrO_6 units, which are the SUs giving the largest contribution to $\Delta\epsilon$ in amorphous Zr silicates.

Using the scheme given by Eqs. (19), (20), (21) and (23), we can now obtain an estimate of ϵ_∞ and ϵ_0 for amorphous $(ZrO_2)_x(SiO_2)_{1-x}$ as a function of Zr composition ($0 < x < 0.5$). Using measured densities for Zr silicates (85), we first calculate ϵ_∞ as a function of x. In this case, the effect of Zr coordination is negligible since the various Zr-centered units have close α values compared to SiO_4 (Table 12). As plotted in Fig. 4, our theoretical values agree very well with available experimental data (83, 85).

In order to apply our scheme for $\Delta\epsilon$, additional information on the cationic coordination is required. We assume that the Si atoms are fourfold coordinated. The coordination of Zr atoms is less well determined. Recent EXAFS measurements (80) tend to show that the average Zr coordination increases from about 4 to about 8 for Zr concentrations increasing from $x \sim 0$ to 0.5. In Fig. 4, we also plot the calculated ϵ_0 for amorphous $(ZrO_2)_x(SiO_2)_{1-x}$ as a function of x, together with the available experimental data (6, 7, 82, 83, 86).

The characteristic parameters used to calculate ϵ_0 change noticeably with the local environment of Zr atoms. Therefore, the indetermination with respect to their coordination leads to a range of possible values for our theoretical values as represented by the dashed band in Fig. 4. We consider several suitable suitable distributions of three representative structural units (ZrO_4, ZrO_6, and ZrO_8). The upper curve delimiting the band in Fig. 4 corresponds to structures entirely composed of ZrO_6 units. The lower curve is for amorphous systems which do not contain any ZrO_6 units. The average Zr coordination varies linearly from four to eight between $x = 0$ and 0.5, with concentrations of ZrO_4 and ZrO_8 SUs varying at most quadratically. Note that the

Table 13. Polarizability (α in bohr^3), characteristic dynamical charge (Z), and characteristic force constant (C in hartree/bohr^2) for MO_6 and MO_8 structural units with M (= Hf, Zr, Ti), extracted from the calculations for the r-MO_2 structures on the one hand, and for the c-MO_2 and $MSiO_4$ structures on the other hand[a]

	HfO_6	ZrO_6	TiO_6	HfO_8	ZrO_8	TiO_8
α	35.28	34.54	33.49	32.21	31.66	32.87
Z	7.19	7.45	8.59	6.77	6.95	7.70
C	0.1278	0.1050	0.0437	0.1630	0.1418	0.0778

[a]The parameters extracted from the $MSiO_4$ structures take into account the values already obtained for SiO_4 SUs which are reported in Table 12.

upper part of the band matches well the recent experimental data (82, 83). The earlier data (6, 7, 86) cannot be explained. Figure 4 shows that, for a sufficient amount of ZrO_6 units, values of ϵ_0 at intermediate x can indeed be larger than estimated from a linear interpolation between SiO_2 and $ZrSiO_4$. However, in agreement with recent experiments (82, 83), our theory indicates that the extent of this effect is more limited than previously assumed (6, 7, 80).

Our scheme could also be applied to Hf and Ti silicates which are very similar to Zr silicates, provided that the value of the characteristic parameters are adapted. In this respect, the comparison between the various crystalline oxides and silicates carried out in the preceding sections provides very useful informations. Indeed, it is possible to extract the characteristic parameters of MO_6 and MO_8 SUs from the results obtained for the r-MO_2 structures on the one hand, and for the c-MO_2 and $MSiO_4$ structures on the other hand. These values are reported in Table 13.

Note the results in Tables 12 and 13 for ZrO_6 and ZrO_8 structural units are in good agreement despite the fact they have been obtained using almost completely different sets of crystalline systems. The only common system is the zircon crystal. In Table 12, the parameters are extracted from the results for crystalline systems that all include Si-centered SUs; whereas, in Table 13, the reference crystals do not include such structural units (apart from zircon). This increases our confidence in the validity of the scheme.

Basically, all the parameters in Table 13 show a similar trend. On the one hand, the enhancement of the dielectric permittivities (both electronic and static) will be larger for the Ti-centered SUs than for Hf- and Zr-centered ones. On the other hand, the MO_6 units produces a larger enhancement than MO_8 units. Hence, for the amorphous silicates, the same kind of considerations should apply. In particular, for Ti amorphous silicates, the dielectric constants should be considerably larger than for Hf and Zr amorphous silicates. Firstly, for Ti, the MO_6 SUs tend to be more stable (as in rutile) than the MO_8 ones; whereas, for Hf and Zr, the MO_8 SUs prevail. Secondly, all the characteristic parameters of Ti-centered SUs produce a larger enhancement than Hf and Zr ones.

5. CONCLUSIONS

Using density-functional theory, we have investigated the structural, electronic, dynamical, and dielectric properties for a series of high-k materials belonging to the Hf–Si–O, Zr–Si–O, and Ti–Si–O systems. We have considered three different structures (cubic, tetragonal, and rutile) for hafnia, zirconia, and titania (the crystalline oxides), as well as hafnon, zircon, and titanon (the crystalline silicates), and finally the amorphous silicates.

In all the investigated systems, we have found a very good agreement between the parameters of the relaxed atomic structures and the experimental ones (when available). The structural parameters are found to be very similar in Hf- and Zr-based materials. On the contrary, the Ti-based materials show some significant differences with respect to the corresponding Hf and Zr oxides and silicates.

The phonon frequencies at the center of the Brillouin zone, the Born effective charge tensors, and the dielectric permittivity tensors have been obtained using density-functional perturbation theory. For the crystalline systems, the agreement between the calculated phonon frequencies and their corresponding experimental values (when available) was found to be excellent. In all the cases, the differences between the Hf-, Zr-, and Ti-based systems have been analyzed in detail and interpreted in terms of structural changes, the mass ratio, and variations of interatomic force constants.

The Born effective charge tensors present an important anisotropy. For some directions, we have found that these effective charges are larger than the nominal ionic charge, indicating a mixed covalent–ionic bonding between M (= Hf, Zr, Ti) and O atoms, and between Si and O atoms. We have also discussed the effective charges focusing on the changes between the systems containing hafnium, zirconium, and titanium.

We have computed the electronic and static dielectric permittivity constants, and have proposed a detailed analysis of the contributions of individual vibrational modes. The discussion is based on the calculation of mode-effective charges and oscillator strengths. For the tetragonal systems (t-HfO_2, t-ZrO_2, r-HfO_2, r-ZrO_2, r-TiO_2, $HfSiO_4$, $ZrSiO_4$, $TiSiO_4$), it was observed, for directions both parallel and perpendicular to the tetragonal axis, that a single mode contributes for more than 60% of the full ionic contribution. The corresponding eigenvectors, which could be obtained in our first-principle approach, show clearly that the displacement is characterized by M (= Hf, Zr, Ti) and O atoms moving in opposite directions. In the silicates, the displacement of Si atoms in these modes is more than twice smaller than those of the other species, inducing a substantial distortion of the SiO_4 tetrahedra in contradiction to what was previously thought. For all systems, the modifications related to the presence of Zr rather than Hf have been rationalized in terms of the difference in mass between these atoms, variations of interatomic force constants, and changes in structural parameters (minor effect).

For hafnon, zircon, and titanon, the electronic density of states have been calculated. The contributions from Hf 5s and 5p, Zr 4s and 4p, Ti 3s and 3p, and O 2s and

2p are clearly distinguishable. The spread of the latter indicates hybridization with atomic M (= Hf, Zr, Ti) and Si orbitals.

Finally, the dielectric properties of amorphous silicates have been investigated. We have proposed a simple scheme which connects the optical and static dielectric constants of Zr silicates to their underlying microscopic structure. Our theory supports recent experiments which find a close to linear dependence of ϵ_0 on the Zr fraction x, and shows that higher dielectric constants can be achieved by increasing the concentration of ZrO_6 structural units. We have extended these results to Hf and Ti amorphous silicates. We have proposed that the dielectric constants should be considerably larger for Ti-based systems than for Hf and Zr ones because of the predominance of MO_6 in the former and the larger enhancement produced by Ti-centered structural units.

ACKNOWLEDGMENTS

The author wishes to thank Drs. F. Detraux, A. Bongiorno, G. Jun, and X. Rocquefelte, as well as Profs. K. Cho, X. Gonze, and A. Pasquarello who took an active part in the research leading to the results presented in this Chapter. He is also grateful to R. B. van Dover for providing us his results prior to publication. Support is acknowledged from the FNRS-Belgium, the FRFC project (N° 2.4556.99), and the Belgian PAI-5/1/1.

APPENDIX: SYMMETRIES OF THE PHONON MODES

In this appendix, we present the procedure to determine the symmetries of the phonon modes $U_{m\mathbf{q}}(\kappa\alpha)$ at a wave vector $\mathbf{q}$ using group theory. For pedagogic purposes, we focus on the practical aspects without giving the formal justifications of the formulas, which may be found in the literature (88). As an example, we will consider the phonon modes at the Γ point for the fluorite structure (space group $Fm\bar{3}m$, N° 225). This corresponds to the cubic structure for the oxides studied previously.

In the following, we adopt the Seitz notation for the symmetry operations of the crystal:

$$\{\mathbf{S} \mid \mathbf{v}(S)\}, \tag{A.1}$$

where $\mathbf{S}$ is 3×3 a real orthogonal matrix representation of a rotation and $\mathbf{v}(S)$ is a vector which is smaller than any primitive translation vector of the crystal. Applied to the equilibrium position vector of atom κ relative to the origin of the cell τ_κ, this symmetry operation transforms it according to the rule:

$$\{\mathbf{S} \mid \mathbf{v}(S)\}\,\tau_\kappa = \mathbf{S}\tau_\kappa + \mathbf{v}(S) = \tau_{\kappa'} + \mathbf{R}(a), \tag{A.2}$$

where $\mathbf{R}(a)$ is a translation vector of the crystal. The second equality expresses the fact that, because the symmetry operation $\{\mathbf{S} \mid \mathbf{v}(S)\}$ is one which sends the crystal into itself, the lattice site κ must be sent onto an equivalent site which we label κ'.

Table A1. Character table for space group $Fm\bar{3}m$ (N° 225) at the Γ point

	E	4	2	3	$2'$	I	-4	m	-3	m'	Functions
Mult.	1	6	3	8	6	1	6	3	8	6	
A_{1g}	1	1	1	1	1	1	1	1	1	1	$x^2+y^2+z^2$
A_{1u}	1	1	1	1	1	−1	−1	−1	−1	−1	
A_{2g}	1	−1	1	1	−1	1	−1	1	1	−1	
A_{2u}	1	−1	1	1	−1	−1	1	−1	−1	1	
E_g	2	0	2	−1	0	2	0	2	−1	0	$(2z^2-x^2-y^2, x^2-y^2)$
E_u	2	0	2	−1	0	−2	0	−2	1	0	
T_{2u}	3	−1	−1	0	1	−3	1	1	0	−1	
T_{2g}	3	−1	−1	0	1	3	−1	−1	0	1	(xy, xz, yz)
T_{1u}	3	1	−1	0	−1	−3	−1	1	0	1	(x, y, z)
T_{1g}	3	1	−1	0	−1	3	1	−1	0	−1	(J_x, J_y, J_z)

The starting point is determine the space group $G_{\mathbf{q}}$ of the wave vector $\mathbf{q}$. It consists of the symmetry operations of the crystal $\{\mathbf{S} \mid \mathbf{v}(S)\}$ whose purely rotational part $\{\mathbf{S}\}$ have the property:

$$\mathbf{Sq} = \mathbf{q} + \mathbf{G}, \tag{A.3}$$

where $\mathbf{G}$ is a translational vector of the reciprocal lattice. It is clear that $\mathbf{G}$ vanishes if $\mathbf{q}$ lies inside the first Brillouin zone, and that it can only be non-zero if $\mathbf{q}$ lies on the boundary of the zone. For our example, since we consider the Γ point, the space group is simply the space group of the crystal.

The next step is to obtain the character table for the space group $G_{\mathbf{q}}$. The various tables for all space groups and special points can be found in books such as ref. (89). Alternatively, the Bilbao Crystallographic Server (90) provides all the tables for the Γ point. For our example, the character table is given in Table A1.

The symmetries of phonon modes are related to the transformation properties of the displacement vectors $U_{m\mathbf{q}}(\kappa\alpha)$. In group theoretical terms, this implies to take direct product of the irreducible representations for the vector (x, y, z) with those of the various atomic sites.

First, we need to find the irreducible representations χ_V of the vector (x, y, z). For our example, we see in Table A1 that:

$$\chi_V = F_{1u}. \tag{A.4}$$

Second, each atomic site is also characterized by one or more symmetry operations that map the atomic site onto itself. The collection of these symmetry operations define the site group (usually labeled using Wyckoff notation). The site group can be one of the 32 crystallographic point groups and must be a subgroup of the space group. For each site, the characters $\chi_{\text{atomic site}}$ represent the number of atoms that are invariant under the symmetry operations of the group. The irreducible representations need to be found for each site. For our example, the Zr and O atoms occupy 4a and 8c

Wyckoff sites, respectively. We find that:

$$\begin{aligned} \chi_{\text{atomic site } 4a} &= A_{1g} \\ \chi_{\text{atomic site } 8c} &= A_{1g} \oplus A_{2u} \end{aligned} \tag{A.5}$$

Finally, the symmetries of the phonon modes are found by taking the direct product of chi_V with $\chi_{\text{atomic sites}}$. For our example, we have that:

$$\begin{aligned} \chi_V \otimes \chi_{\text{atomic site } 4a} &= F_{1u} \otimes A_{1g} = F_{1u} \\ \chi_V \otimes \chi_{\text{atomic site } 8c} &= F_{1u} \otimes (A_{1g} \oplus A_{2u}) = F_{1u} \oplus F_{2g} \end{aligned} \tag{A.6}$$

Hence, the theoretical group analysis predicts the following irreducible representations of optical and acoustical zone-center modes for the cubic phase:

$$\Gamma = \underbrace{F_{2g}}_{\text{Raman}} \oplus \underbrace{F_{1u}}_{\text{IR}} \oplus \underbrace{F_{1u}}_{\text{Acoustic}} . \tag{A.7}$$

The final step is to assign each phonon mode m individually, that is to find its characters $\chi_{m\mathbf{q}}(\{\mathbf{S} \mid \mathbf{v}(S)\})$ with respect to the various symmetry operations of $G_{\mathbf{q}}$. For non-degenerate modes, it can be demonstrated (88) that:

$$\begin{aligned} \chi_{m\mathbf{q}}(\{\mathbf{S} \mid \mathbf{v}(S)\}) &= \sum_{\kappa\kappa'} \sum_{\alpha\beta} U_{m\mathbf{q}}(\kappa\alpha)\, T_{\alpha\beta}\, U_{m\mathbf{q}}(\kappa'\beta)\delta(\kappa, F_0(\kappa'; R)), \\ \text{with } T_{\alpha\beta} &= S_{\alpha\beta} e^{i\mathbf{q}\cdot[\tau_\kappa - \mathbf{S}\tau_\kappa]}, \end{aligned} \tag{A.8}$$

where $F_0(\kappa'; S)$ is the label of the atom to which the atom κ' is brought by the symmetry operation $\{\mathbf{S} \mid \mathbf{v}(S)\}$. The δ expresses that we only need to taken into account those atoms κ' that map on to atom κ by the symmetry operation. In case of degeneracy, the sum in Eq. (A.8) must be extended to all the degenerate modes.

By comparing the characters $\chi_{m\mathbf{q}}(\{\mathbf{S} \mid \mathbf{v}(S)\})$ with Table A1, it is then quite straightforward to assign the various phonon modes. In the end, we can double check the assignments obtained in this way agree with the irreducible representations of $\chi_V \otimes \chi_{\text{atomic sites}}$.

REFERENCES

1. G.D. Wilk, R.M. Wallace, J.M. Anthony, High-k gate dielectrics: Current status and materials properties considerations, *J. Appl. Phys.* **89**(10), 5243–5275 (2001).
2. S.A. Campbell, D.C. Gilmer, X.C. Wang, M.T. Hsieh, H.S. Kim, W.L. Gladfelter, J.H. Yan, MOSFET transistors fabricated with high permitivity TiO_2 dielectrics, *IEEE Trans. Electron Devices* **44**(1), 104–109 (1997).
3. C.J. Taylor, D.C. Gilmer, D.G. Colombo, G.D. Wilk, S.A. Campbell, J.Roberts, W.L. Gladfelter, Does chemistry really matter in the chemical vapor deposition of titanium dioxide? Precursor and kinetic effects on the microstructure of polycrystalline films, *J. Am. Chem. Soc.* **121**(22), 5220–5229 (1999).
4. J. Zhang, J.S. Yuan, Y. Ma, A.S. Oates, Design optimization of stacked layer dielectrics for minimum gate leakage currents, *Solid State Electron.* **44**(12), 2165–2170 (2000).

5. M. Kadoshima, M. Hiratani, Y. Shimamoto, K. Torii, H. Miki, S. Kimura, T. Nabatame, Rutile-type TiO_2 thin film for high-k gate insulator, *Thin Solid Films* **424**(2), 224–228 (2003).
6. G.D. Wilk, R.M. Wallace, Stable zirconium silicate gate dielectrics deposited directly on silicon, *Appl. Phys. Lett.* **76**, 112–114 (2000).
7. G.D. Wilk, R.M. Wallace, J.M. Anthony, Hafnium and zirconium silicates for advanced gate dielectrics, *J. Appl. Phys.* **87**, 484–492 (2000).
8. P.H. Giauque, H.B. Cherry, M.A. Nicolet, Thermal stability of amorphous $Ti_3Si_1O_8$ thin films, *Microelectron Eng.* **55**(1–4), 183–188 (2001).
9. D.K. Sarkar, E. Desbiens, M.A. El Khakani, High-k titanium silicate dielectric thin films grown by pulsed-laser deposition, *Appl. Phys. Lett.* **80**(2), 294–296 (2002).
10. R.C. Smith, N. Hoilien, C. Dykstra, S.A. Campbell, J.T. Roberts, W.L. Gladfelter, Cvd of $Ti_xSi_{1-x}O_2$ films: Precursor chemistry impacts film composition, *Chem. Vapor Deposition* **9**(2), 79–86 (2003).
11. P. Hohenberg, W. Kohn, Inhomogeneous electron gas, *Phys. Rev.* **136**, B864–B871 (1964).
12. W. Kohn, L.J. Sham, Self-consistent equations including exchange and correlation effects, *Phys. Rev.* **140**, A1133–A1138 (1965).
13. W.E. Pickett, Pseudopotential methods in condensed matter applications, *Comput. Phys. Rep.* **9**, 115–197 (1989).
14. M.C. Payne, M.P. Teter, D.C. Allan, T.A. Arias, J.D. Joannopoulos, Iterative minimization techniques for ab initio total-energy calculations: Molecular-dynamics and conjugate gradients, *Rev. Mod. Phys.* **64**, 1045–1097 (1992).
15. S. Baroni, S. de Gironcoli, A. Dal Corso, P. Giannozzi, Phonons and related crystal properties from density-functional perturbation theory, *Rev. Mod. Phys.* **73**, 515–562 (2001).
16. X. Gonze, First-principles responses of solids to atomic displacements and homogeneous electric fields: Implementation of a conjugate-gradient algorithm, *Phys. Rev. B* **55**, 10337–10354 (1997).
17. X. Gonze, C. Lee, Dynamical matrices, born effective charges, dielectric permittivity tensors, and interatomic force constants from density-functional perturbation theory, *Phys. Rev. B* **55**, 10355–10368 (1997).
18. X. Gonze, J.M. Beuken, R. Caracas, F. Detraux, M. Fuchs, G.M. Rignanese, L. Sindic, M. Verstraete, G. Zerah, F. Jollet, M. Torrent, A. Roy, M. Mikami, P. Ghosez, J.Y. Raty, D.C. Allan, First-principles computation of material properties: the ABINIT software project, *Comp. Mater. Sci.* **25**, 478–492 (2002). http://www.abinit.org.
19. J.P. Perdew, Y. Wang, Accurate and simple analytic representation of the electron–gas correlation-energy, *Phys. Rev. B* **45**, 13244–13249 (1992).
20. D.M. Ceperley, B.J. Alder, Ground state of electron gas by stochastic method, *Phys. Rev. Lett.* **45**, 566–569 (1980).
21. N. Troullier, J.L. Martins, Efficient pseudopotentials for plane-wave calculations, *Phys. Rev. B* **43**, 1993–2006 (1991).
22. M. Teter, Additional condition for transferability in pseudopotentials, *Phys. Rev. B* **48**, 5031–5041 (1993).
23. L. Kleinman, D.M. Bylander, Efficacious form for model pseudopotentials, *Phys. Rev. Lett.* **48**, 1425 (1982).
24. H.J. Monkhorst, J.D. Pack, Special points for Brillouin-zone integration, *Phys. Rev. B* **13**, 5188–5192 (1976).
25. P. Duran, C. Pascual, Phase equilibria and ordering the system HfO_2-Yb_2O_3, *J. Mater. Sci.* **19**, 1178–1184 (1984).
26. G. Teufer, The crystal structure of tetragonal ZrO_2, *Acta Cryst.* **15**, 1187–1187 (1962).
27. R. Ruh, H.J. Garrett, R.F. Domagala, N.M. Tallen, System zirconia-hafnia, *J. Am. Ceram. Soc.* **51**, 23–27 (1968).

28. P. Aldebert, J.P. Traverse, Structure and ionic mobility of zirconia at high temperature, *J. Am. Ceram. Soc.* **68**, 34–40 (1985).
29. J.C. Slater, Atomic radii in crystals, *J. Chem. Phys.* **39**, 3199–3204 (1964).
30. D.R. Lide, *CRC Handbook for Chemistry and Physics*, 76th Edition (CRC Press, Boca Raton, FL, 1995).
31. E.J. Little, M.M. Jones, A complete table of electronegativities, *J. Chem. Educ.* **37**, 231–233 (1960).
32. C. Lee, Ph. Ghosez, X. Gonze, Lattice-dynamics and dielectric-properties of incipient ferroelectric TiO_2 rutile, *Phys. Rev. B* **50**, 13379–13387 (1994).
33. C.Y. Lee, X. Gonze, Dielectric-constants and born effective charges of TiO_2 rutile, *Phys. Rev. B* **49**(20), 14730–14731 (1994).
34. K. Parlinski, Z.Q. Li, Y. Kawazoe, First-principles determination of the soft mode in cubic ZrO_2, *Phys. Rev. Lett.* **78**(21), 4063–4066 (1997).
35. B. Králik, E.K. Chang, S.G. Louie, Structural properties and quasiparticle band structure of zirconia, *Phys. Rev. B* **57**, 7027–7036 (1998).
36. M.W. Finnis, A.T. Paxton, M. Methfessel, M. van Schilfgaarde. Crystal structures of zirconia from first principles and self-consistent tight binding, *Phys. Rev. Lett.* **81**(23), 5149–5152 (1998).
37. G. Jomard, T. Petit, A. Pasturel, L. Magaud, G. Kresse, J. Hafner, First-principles calculations to describe zirconia pseudopolymorphs, *Phys. Rev. B* **59**(6), 4044–4052 (1999).
38. J.E. Lowther, J.K. Dewhurst, J.M. Leger, J. Haines, Relative stability of ZrO_2 and HfO_2 structural phases, *Phys. Rev. B* **60**(21), 14485–14488 (1999).
39. R. Asahi, Y. Taga, W. Mannstadt, A.J. Freeman, Electronic and optical properties of anatase TiO_2, *Phys. Rev. B* **61**(11), 7459–7465 (2000).
40. M. Mikami, S. Nakamura, O. Kitao, H. Arakawa, X. Gonze, First-principles study of titanium dioxide: Rutile and anatase, *Jpn. J. Appl. Phys. 2*, **39**(8B), L847–L850 (2000).
41. G.-M. Rignanese, F. Detraux, X. Gonze, A. Pasquarello, First-principles study of dynamical and dielectric properties of tetragonal zirconia, *Phys. Rev. B* **64** 1–7:134301, (2001).
42. A.A. Demkov, Investigating alternative gate dielectrics: A theoretical approach, *Phys. Status Solidi B* **226**, 57–67 (2001).
43. X. Zhao, D. Vanderbilt, First-principles study of structural, vibrational, and lattice dielectric properties of hafnium oxide, *Phys. Rev. B* **65**(1–4) :233106, (2002).
44. X. Zhao, D. Vanderbilt, Phonons and lattice dielectric properties of zirconia, *Phys. Rev. B* **65**(1–10) :075105, (2002).
45. J. Muscat, V. Swamy, N. M. Harrison, First-principles calculations of the phase stability of TiO_2, *Phys. Rev. B* **65**(22)(1–15):224112, (2002).
46. M. Mikami, S. Nakamura, O. Kitao, H. Arakawa, Lattice dynamics and dielectric properties of TiO_2 anatase: A first-principles study, *Phys. Rev. B* **66**(15):155213, 1–6 (2002).
47. N.N. Greenwood, A. Earnshaw, *Chemistry of Elements*, 2nd Edition (Butterworth-Heinemann, Oxford, UK 1997).
48. J. Wang, H.P. Li, R. Stevens, Hafnia and hafnia-toughened ceramics, *J. Mater. Sci.* **27**, 5397–5430 (1992).
49. W. Zhong, D. King-Smith, D. Vanderbilt, Giant LO–TO splitting in perovskite ferroelectrics, *Phys. Rev. Lett.* **72**, 3618–3621 (1994).
50. Ph. Ghosez, J.-P. Michenaud, X. Gonze, Dynamical atomic charges: The case of ABO_3 compounds, *Phys. Rev. B* **58**, 6224–6240 (1998).
51. C. Lee, X. Gonze, Lattice-dynamics and dielectric-properties of SiO_2 stishovite, *Phys. Rev. Lett.* **72**, 1686–1689 (1994).
52. X. Gonze, J.-C. Charlier, D.C. Allan, M.P. Teter, Interatomic force-constants from first principles—the case of alpha-quartz, *Phys. Rev. B* **50**, 13035–13038 (1994).
53. P. Giannozzi, Gironcoli. S. de, P. Pavone, S. Baroni, Ab initio calculation of phonon dispersions in semiconductors, *Phys. Rev. B* **43**, 7231–7242 (1991).

54. J.G. Traylor, H.G. Smith, R.M. Nicklow, M.K. Wilkinson, Lattice dynamics of rutile, *Phys. Rev. B* **3**(10), 3457–3472 (1971).
55. A. Feinberg, C.H. Perry, Structural disorder and phase transitions in ZrO_2-Y_2O_3 system, *J. Phys. Chem. Solids* **42**, 513–518 (1981).
56. T. Hirata, E. Asari, M. Kitajima, Infrared and raman-spectroscopic studies of ZrO_2 polymorphs doped with Y_2O_3 or CeO_2, *J. Solid State Chem.* **110**, 201–207 (1994).
57. C. Pecharromán, M. Ocaña, C.J. Serna, Optical constants of tetragonal and cubic zirconias in the infrared, *J. Appl. Phys.* **80**, 3479–3483 (1996).
58. P. Bouvier, G. Lucazeau, Raman spectra and vibrational analysis of nanometric tetragonal zirconia under high pressure, *J. Phys. Chem. Solids* **61**, 569–578 (2000).
59. K. Negita, Lattice vibrations and cubic to tetragonal phase transition in ZrO_2, *Acta. Metall.* **37**, 313–317 (1989).
60. K. Negita, H. Takao, Condensations of phonons at the tetragonal to monoclinic phase transition in ZrO_2, *J. Phys. Chem. Solids* **50**, 325–331 (1989).
61. C. Pecharromán, J.E. Iglesias, Effective dielectric-properties of packed mixtures of insulator particles, *Phys. Rev. B* **49**, 7137–7147 (1994).
62. K. Kukli, J. Ihanus, M. Ritala, M. Leskela, Tailoring the dielectric properties of HfO_2–Ta_2O_5 nanolaminates, *Appl. Phys. Lett.* **68**, 3737–3739 (1996).
63. E.P. Gusev, E. Cartier, D.A. Buchanan, M. Gribelyuk, M. Copel, H. Okorn-Schmidt, C. D'Emic, Ultrathin high-k metal oxides on silicon: processing, characterization and integration issues, *Micorelectron. Eng.* **59**, 341–349 (2001).
64. D.W. Liu, C.H. Perry, R.P. Ingel, Infrared spectra in nonstoichiometric yttria-stabilized zirconia mixed crystals at elevated temperatures, *J. Appl. Phys.* **64**, 1413–1417 (1988).
65. D.L. Wood, K. Nassau, Refractive index of cubic zirconia stabilized with yttria, *Appl. Opt.* **21**, 2978–2981 (1982).
66. R.H. French, S.J. Glass, F.S. Ohuchi, Y.-N. Xu, W.Y. Ching, Experimental and theoretical determination of the electronic-structure and optical-properties of 3 phases of ZrO_2, *Phys. Rev. B* **49**, 5133–5142 (1994).
67. M.T. Lanagan, J.K. Yamamoto, A. Bhalla, S.G. Sankar, The dielectric properties of yttria-stabilized zirconia, *Mater. Lett.* **7**, 437–440 (1989).
68. A. Dwivedi, A.N. Cormack, A computer-simulation study of the defect structure of calcia-stabilized zirconia, *Phil. Mag.* **61**, 1–22 (1990).
69. R.A. Parker, Static dielectric constant of rutile (TiO_2), 1.6-1060 k, *Phys. Rev.* **124**(6), 1719–1722 (1961).
70. G.A. Samara, P.S. Peercy, Pressure and temperature dependence of the static dielectric constants and raman spectra of TiO_2 (rutile), *Phys. Rev. B* **7**(3), 1131–1148 (1973).
71. J.A. Speer, B.J. Cooper, Crystal structure of synthetic hafnon, $HfSiO_4$, comparison with zircon and the actinide orthosilicates, *American Mineralogist* **67**, 804–808 (1982).
72. G.-M. Rignanese, X. Gonze, A. Pasquarello, First-principles study of structural, electronic, dynamical, and dielectric properties of zircon, *Phys. Rev. B* **63**:104305, 1–7 (2001).
73. Z. Mursic, T. Vogt, H. Boysen, F. Frey, Single-crystal neutron-diffraction study of metamict zircon up to 2000 k, *J. Appl. Crystallogr.* **25**, 519–523 (1992).
74. X. Gonze, D.C. Allan, M.P. Teter, Dielectric tensor, effective charges, and phonons in alpha-quartz by variational density-functional perturbation-theory, *Phys. Rev. Lett.* **68**, 3603–3606 (1992).
75. J.H. Nicola, H.N. Rutt, A comparative study of zircon ($ZrSiO_4$) and hafon ($HfSiO_4$) raman spectra, *J. Phys. C: Solid State Phys.* **7**, 1381–1386 (1974).
76. P.W.O. Hoskin, K.A. Rodgers, Raman spectral shift in the isomorphous series $(Zr_{1-x}Hf_x)SiO_4$, *Eur. J. Solid State Inorg. Chem.* **23**, 1111–1121 (1996).
77. P. Dawson, M.M. Hargreave, G.R. Wilkinson, The vibrational spectrum of zircon ($ZrSiO_4$), *J. Phys. C: Solid State Phys.* **4**, 240–256 (1971).

78. F. Gervais, B. Piriou, F. Cabannes, Anharmonicity in silicate crystals: Temperature dependence of A_u type vibrational modes in $ZrSiO_4$ and $LiAlSi_2O_6$, *J. Phys. Chem. Solids* **34**, 1785–1796 (1973).
79. C. Pecharromán, M. Ocaña, P. Tartaj, C.J. Serna, Infrared optical-properties of zircon, *Mater. Res. Bull.* **29**, 417–426 (1994).
80. G. Lucovsky, G.B.Jr. Rayner, Microscopic model for enhanced dielectric constants in low concentration SiO_2-rich noncrystalline Zr and Hf silicate alloys, *Appl. Phys. Lett.* **77**, 2912–2914 (2000).
81. H.A. Kurtz, R.A.B. Devine, Role of bond coordination and molecular volume on the dielectric constant of mixed-oxide compounds, *Appl. Phys. Lett.* **79**, 2342–2344 (2001).
82. W.-J. Qi, R. Nieh, E. Dharmarajan, B.H. Lee, Y. Jeon, L. Kang, K. Onishi, J.C. Lee, Ultrathin zirconium silicate film with good thermal stability for alternative gate dielectric application, *Appl. Phys. Lett.* **77**, 1704–1706 (2000).
83. R.B. van Dover, L. Manchanda, M.L. Green, G. Wilk, E. Garfunkel, B. Busch, unpublished, (2001).
84. G.-M. Rignanese, F. Detraux, X. Gonze, A. Bongiorno, A. Pasquarello, Dielectric constants of Zr silicates: A first-principles study, *Phys. Rev. Lett.* **89**:117601, 1–4 (2002).
85. M. Nogami, Glass preparation of the ZrO_2–SiO_2 system by the sol-gel process from metal alkoxide, *J. Non-Cryst. Solids* **69**, 415–423 (1985).
86. V. Misra, unpublished, (2001).
87. A.K. Varshneya, *Fundamental of Inorganic Glasses*, (Academic Press Inc., San Diego, CA (1994).
88. A.A. Maradudin, S.H. Vosko, Symmetry properties of the normal vibrations of a crystal, *Rev. Mod. Phys.* **40**, 1–37 (1968).
89. S.C. Miller, W.S. Love, *Tables of Irreducible Representations of Space Groups and Co-Representations of Magnetic Space Groups* (Pruett Press, Boulder, CO, 1967).
90. E. Kroumova, J.M. Perez-Mato, M.I. Aroyo, S. Ivantchev, G. Madariaga, H. Wondratschek, The bilbao crystallographic server: a web site with crystallographic tools using the international tables for crystallography, in: *18th European Crystallographic Meeting* (1998). http://www.cryst.ehu.es.